Research Paper

GEOSPHERE

GEOSPHERE, v. 17

https://doi.org/10.1130/GES02243.1

13 figures; 6 tables; 1 supplemental file

CORRESPONDENCE: bridget@wisc.edu

CITATION: Garnier, B., Tikoff, B., Flores, O., Jicha, B., DeMets, C., Cosenza-Muralles, B., Hernandez, D., Marroquin, G., Mixco, L., and Hernandez, W., 2020, An integrated structural and GPS study of the Jalpatagua fault, southeastern Guatemala: Geosphere, v. 17, https://doi.org/10.1130/GES02243.1.

Science Editor: David E. Fastovsky
Associate Editor: Craig H. Jones

Received 7 February 2020
Revision received 21 September 2020
Accepted 28 October 2020

An integrated structural and GPS study of the Jalpatagua fault, southeastern Guatemala

Bridget Garnier[1], Basil Tikoff[1], Omar Flores[2], Brian Jicha[1], Charles DeMets[1], Beatriz Cosenza-Muralles[1,3], Douglas Hernandez[4], Griselda Marroquin[4], Luis Mixco[4], and Walter Hernandez[4]

[1]Department of Geoscience, University of Wisconsin–Madison, 1215 West Dayton St., Madison, Wisconsin 53706, USA
[2]Centro de Estudios Superiores de Energías y Minas–Facultad de Ingeniería, Universidad de San Carlos, Ciudad Universitaria, Zona 12, Edificio T-1, tercer nivel, Ciudad de Guatemala 01012, Guatemala
[3]Instuto de Invesgación en Ciencias Físicas y Matemácas, Escuela de Ciencias Físicas y Matemácas, Universidad de San Carlos, Ciudad Universitaria, Zona 12, Edificio T-1, segundo nivel, Ciudad de Guatemala, Guatemala
[4]Dirección del Observatorio, Ministerio de Medio Ambiente y Recursos Naturales, Km. 5½ carretera a Santa Tecla, colonio y calle Las Mercedes, San Salvador, El Salvador

ABSTRACT

The Jalpatagua fault in Guatemala accommodates dextral movement of the Central America forearc. We present new global positioning system (GPS) data, minor fault analysis, geochronological analyses, and analysis of lineaments to characterize deformation along the fault and near its terminations. Our data indicate that the Jalpatagua fault terminates at both ends into extensional regions. The western termination occurs near the Amatitlan caldera and the southern extension of the Guatemala City graben, as no through-going structures were observed to continue west into the active volcanic arc. Along the Jalpatagua fault, new and updated GPS site velocities are consistent with a slip rate of 7.1 ± 1.8 mm yr^{-1}. Minor faulting along the central section of the fault includes: (1) N-S–striking normal faults accommodating E-W elongation; and (2) four sets of strike-slip faults (oriented 330°, 020°, 055°, and 295°, parallel to the Jalpatagua fault trace). Minor fault arrays support dextral movement along a major fault in the orientation of the Jalpatagua fault. GPS and fault data indicate that the Jalpatagua fault terminates to the east near the Guatemala–El Salvador border. Data delineate a pull-apart basin southeast of the fault termination, which is undergoing transtension as the Jalpatagua fault transitions into the El Salvador fault system to the east. Within the basin, minor faulting and lineations trend to the NW and accommodate NE-directed elongation. This faulting differs from E-W elongation observed along the Jalpatagua fault and is more similar to minor faults within the El Salvador fault system.

Bridget Garnier https://orcid.org/0000-0001-9622-8269

INTRODUCTION

Moving forearc slivers typically result from strain partitioning due to oblique convergence between the subducting and overriding plates (e.g., Fitch, 1972; Jarrard, 1986; McCaffrey, 1992). In these cases, strike-slip faults are typically found within or adjacent to an active volcanic arc (e.g., de Saint Blanquat et al., 1998; Sieh and Natawidjaja, 2000; Garibaldi et al., 2016). While forearc slivers are common features around the world, the way in which strike-slip motion is accommodated at their boundaries varies greatly between each system. A singular strike-slip fault occurs in the Sumatra fault system in Indonesia (e.g., Sieh and Natawidjaja, 2000), series of en echelon faults are interpreted to occur in El Salvador (e.g., Garibaldi et al., 2016; Martínez-Díaz et al., 2004), and a complicated fault network containing coeval areas of transpression and transtension are present along the Andean fault system in southern Chile (e.g., Grocott and Taylor, 2002). It is unclear what guides the type of faulting that will accommodate forearc movement in each setting, particularly in the presence of an active volcanic arc, which complicates the rheological behavior of the upper crust (Martin et al., 2014).

The Central American moving forearc, which may have resulted from multiple factors within an uncoupled subduction zone, provides an opportunity to investigate along-strike variations in the character of strike-slip faulting. The forearc region in Central America accommodates dextral movement and extends from Costa Rica to southern Guatemala, along the active volcanic arc, and parallels the Middle America Trench (Fig. 1; DeMets, 2001; Guzmán-Speziale et al., 2005; Lyon-Caen et al., 2006; Franco et al., 2012). The dextral forearc fault system is the widest in Nicaragua, with NE-oriented sinistral faults that suggest bookshelf faulting may accommodate dextral movement rather than arc-parallel dextral faults (NFS in Fig. 1; Weinberg, 1992; La Femina et al., 2002). In El Salvador, the El Salvador fault system progressively narrows to the northwest and consists of a zone of right-stepping strike-slip faults, related pull-apart basins, active volcanoes, and calderas (ESFS in Fig. 1; Martínez-Díaz et al., 2004; Alvarado et al., 2011; Canora et al., 2014; Alonso-Henar et al., 2014, 2015, 2017; Garibaldi et al., 2016; Staller et al., 2016). In southeastern Guatemala, dextral movement occurs on the Jalpatagua fault, which begins near the Guatemala–El Salvador border and continues for nearly 70 km before terminating at the southern extension of the Guatemala City graben (JF in Fig. 1). The Jalpatagua fault is arguably the termination of the forearc fault system, as no clear evidence for discrete strike-slip faulting is apparent geologically or geodetically (Ellis et al., 2019) west of Guatemala City.

The goal of this study was to document and interpret deformation along and near the Jalpatagua fault system. The Jalpatagua fault is relatively unstudied (Carr, 1974, 1976; Plafker, 1976; Duffield et al., 1992; Authemayou et al., 2011), likely because of poor exposure resulting from abundant vegetation and tropical weathering. Here, we present new global positioning system (GPS) data and an associated elastic block model, minor fault analysis, geochronological analyses, and analysis of lineaments associated with the Jalpatagua fault. Minor faulting supports dextral movement along the

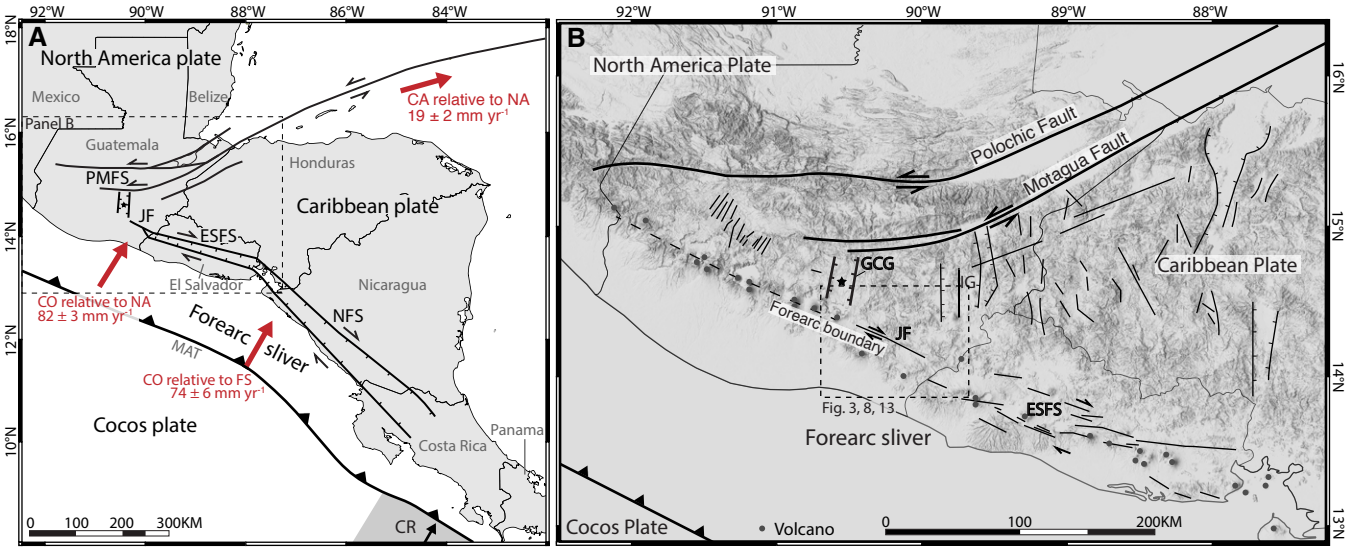

Figure 1. (A) Overview of the major tectonic plates, plate velocities, and fault systems in northern Central America. Dashed gray box indicates the area of panel B. The general boundaries of the dextral forearc fault system extend from Guatemala to Costa Rica and are based on Authemayou et al. (2011). The plate velocities and 95% uncertainties were determined using angular velocities from table 1 of Ellis et al. (2019). Plate names and boundaries of major fault systems are abbreviated as follows: CA—Caribbean plate; CO—Cocos plate; FS—Central America forearc sliver; NA—North American plate; MAT—Middle America Trench; PMFS—Polochic-Motagua fault system; JF—Jalpatagua fault; ESFS—El Salvador fault system; NFS—Nicaragua fault system; CR—Cocos Ridge. Black star represents the location of Guatemala City, within the Guatemala City graben. (B) 20 m digital elevation model of Guatemala and El Salvador (OpenStreetMap contributors, 2015) annotated with major faults and features. Black star represents Guatemala City within the Guatemala City graben (GCG). Dashed gray box indicates the area of Figures 2, 8, and 13. IG—Ipala graben.

Jalpatagua fault, although with along-strike variations. In southeastern Guatemala, the Jalpatagua fault terminates at its eastern end into a complex zone of faulting associated with a step-over in the El Salvador fault system. The fault terminates at its western end near the Amatitlan caldera and the southern end of the Guatemala City graben.

TECTONIC FRAMEWORK OF SOUTHEASTERN GUATEMALA

Geodetic Constraints

Deformation in southern Guatemala is the result of the relative movements of the North America, Caribbean, and Cocos plates, which meet in a zone of diffuse deformation in southwestern Guatemala (Fig. 1; Lyon-Caen et al., 2006; Alvarez-Gomez et al., 2008; Rodriguez et al., 2009; Authemayou et al., 2011; Franco et al., 2012). The North America–Caribbean plate boundary is defined by the arcuate left-lateral Polochic-Motagua fault system in central Guatemala, as the North America plate moves ~18 mm yr^{-1} westward relative to the Caribbean plate (Ellis et al., 2019; also see Weyl, 1980; Mann et al., 2007; Lyon-Caen et al., 2006; DeMets et al., 2010; Authemayou et al., 2012; Franco et al., 2012). The Cocos plate subducts ~73–76 mm yr^{-1} (toward N27.5–30°E) beneath the forearc sliver of the Caribbean plate off the southwest coast of Central America (Ellis et al., 2019). Within this system, an active volcanic arc (Central American volcanic arc) and the dextral moving forearc extend from western Guatemala to Costa Rica, parallel to the Middle America Trench.

Forearc movement may result from: (1) strain partitioning from oblique convergence between the Cocos and Caribbean plates in an uncoupled subduction zone, (2) pull from the North America plate where the forearc is pinned and moves to the northwest as the Caribbean plate moves eastward, (3) westward push from a collision of the Cocos Ridge beneath the Costa Rican forearc, and/or (4) a combination of pushing of the Cocos Ridge and forearc pinning (DeMets, 2001; Lyon-Caen et al., 2006; La Femina et al., 2009; Alvarez-Gomez et al., 2008, 2019; Franco et al., 2012; Staller et al., 2016). In Guatemala, the Jalpatagua fault defines the forearc boundary, which creates a clear topographic lineament oriented ~295° that parallels the volcanic arc and the Middle America Trench (Fig. 1; Williams, 1960; Carr, 1974, 1976; Weyl, 1980; Wunderman and Rose, 1984; Alvarez-Gomez et al., 2008, 2019; Authemayou et al., 2011).

Based on a regional elastic block model that best fits a new 200+ station GPS velocity field in northern Central America and southern Mexico,

Ellis et al. (2019) estimated that the Central America forearc sliver moves 7.6 ± 2.1 mm yr^{-1} toward N75°W ± 12° relative to the lithosphere inland from the Jalpatagua fault, ~25% slower than the ~10 mm yr^{-1} Jalpatagua fault slip rate estimated by Lyon-Caen et al. (2006) from the first GPS measurements in southern Guatemala. Farther east, the new block model predicts that the rate of dextral forearc movement increases to 9.7 ± 1.4 mm yr^{-1} in western El Salvador, 10.3 ± 1.2 mm yr^{-1} in central El Salvador along the El Salvador fault system, and 12.5 ± 1.0 mm yr^{-1} across the Nicaraguan volcanic arc. Along the El Salvador fault zone, the forearc sliver motion is accommodated by approximately E-W strike-slip faults and NW-SE and N-S secondary normal faults (Fig. 1B; Alvarado et al., 2011; Alonso-Henar et al., 2014, 2015, 2017; Garibaldi et al., 2016; Staller et al., 2016; Ellis et al., 2019), whereas dextral forearc slip in Nicaragua is mostly accommodated across an ~50-km-wide zone of bookshelf faulting on NE-striking sinistral faults (La Femina et al., 2002). West of the Guatemala City graben, which approximates the western terminus of the Jalpatagua fault, Ellis et al. (2019) found almost no velocity gradient across the Central America volcanic arc, consistent with the apparent absence of active, arc-parallel faults west of Guatemala City.

Deformation north of the Jalpatagua fault, in the backarc region, is characterized by approximately E-W extension across multiple N-S–oriented grabens (e.g., Guatemala City graben and Ipala graben; Lyon-Caen et al., 2006; Alvarez-Gomez et al., 2008, 2019; Franco et al., 2012). GPS observations that span the entire ~700-km-wide extending region north of the volcanic arc–forearc boundary indicate a net divergence rate of 7.1 ± 1.8 mm yr^{-1} between the undeforming Caribbean plate in central Honduras and the eastern edge of the Guatemala City graben (Ellis et al., 2019). This divergence rate includes 1.8 mm yr^{-1} of divergence across the Ipala graben and another 5 mm yr^{-1} variously distributed within the Chortis and Ipala blocks east and west of the Ipala graben. The distributed extension north of the volcanic arc, which may be caused by eastward movement of the Caribbean plate (Fig. 1; Guzmán-Speziale, 2001; Lyon-Caen et al., 2006; Alvarez-Gomez et al., 2008, 2019; Rodriguez et al., 2009; Franco et al., 2012), results in the gradual westward decrease in slip rate along the Motagua-Polochic fault system as well in the Central America forearc boundary. Forearc boundary slip rates decrease as slip is transferred northward into the active grabens.

Structural Constraints

Early work by Williams (1960) and Carr (1974, 1976) established a right-lateral sense of motion along the Jalpatagua fault. Their evaluation was based on conjugate left-lateral faults in the area, NW-oriented en échelon fractures in El Salvador, dextral river valley (Los Esclavos River; Fig. 2) offsets of ~9–12 km along the lineament, and focal mechanisms from the San Salvador 1963 earthquake indicating right-lateral movement on a 295° orientation. Carr (1974) also noted the 500-m-high fault scarp of the Jalpatagua fault north of the town of Jalpatagua, which he suggested was created by subsidence related to eruption of pyroclastic material.

Later work by Eggers (1971) and Wunderman and Rose (1984) on the Lake Amatitlan caldera to the west, near the westernmost terminus of the Jalpatagua fault, suggested that the Jalpatagua fault continues through the caldera, as evidenced by the linearity of Lake Amatitlan and 1 km offsets of outer rim faults on the east side of the caldera. Additionally, young N-S–striking faults were mapped within the caldera (Eggers, 1971).

Reynolds (1977, 1980, 1987) completed field mapping of three quadrangles north of the Jalpatagua fault near the town of Cuilapa. His work focused on the Santa Rosa de Lima caldera. He suggested that the southern portion of the caldera intersects the Jalpatagua fault and is deflected around the edge of the caldera.

Investigations by Duffield et al. (1992) on the Tecuamburro volcano, south of the Jalpatagua fault and near the Los Esclavos River, reported evidence for cataclasis along the Jalpatagua fault. In this locality, lavas and tuffs are sheared into cataclastic breccias, and nonwelded tuffs are pulverized into rock flour along the fault. The Los Esclavos River has also been used as a geomorphic feature by multiple studies to determine fault offset (Duffield et al., 1992; Authemayou et al., 2011). Authemayou et al. (2011) calculated 6.5–8.7 km of dextral offset along the Jalpatagua fault using the large bend in the Los Esclavos River along the fault trace. These authors also estimated that a decapitated alluvial fan near Oratorio indicates 1.2 ± 0.2 km of dextral offset. While nearly all these studies utilized geomorphic analyses using aerial/satellite photos and elevation maps, Authemayou et al. (2011) was the only study to record fault orientation and lineation measurements (n = 10) related to the Jalpatagua fault, measured within 1 km of the interpreted fault trace. The lack of published structural data highlights the lack of outcrops on or near the Jalpatagua fault.

Stratigraphy along the Jalpatagua Fault and Terminations

We present a general overview of stratigraphy along the Jalpatagua fault, with specific unit correlation provided in the data description section, Table 1, and Figure 3. The stratigraphy of southern Guatemala along the Jalpatagua fault is dominated by Quaternary and Neogene volcanic deposits and reworked sediments that were deposited during multiple periods of volcanic activity within this time period (Koch and McLean, 1975; Bethancourt et al., 1976; Reynolds, 1977, 1980, 1987; Wunderman and Rose, 1984; Duffield et al., 1992; Rose et al., 1999). With numerous eruptive centers in space and time, the stratigraphy is highly variable from location to location, often making unit identification difficult.

There is a distinction between Quaternary and Neogene deposits within the literature and in stratigraphic columns of Guatemala: (1) Quaternary tephras are identified individually; and (2) Neogene deposits are bulked into three formations: the upper Cuscatlán, middle Básalmo, and lower Chalatenango formations (Fig. 3; Williams, 1960; Koch and McLean, 1975; Reynolds, 1980). In general, recent Quaternary tephras, lavas, and reworked deposits are better described, defined, and mapped in the literature due to widespread exposure across

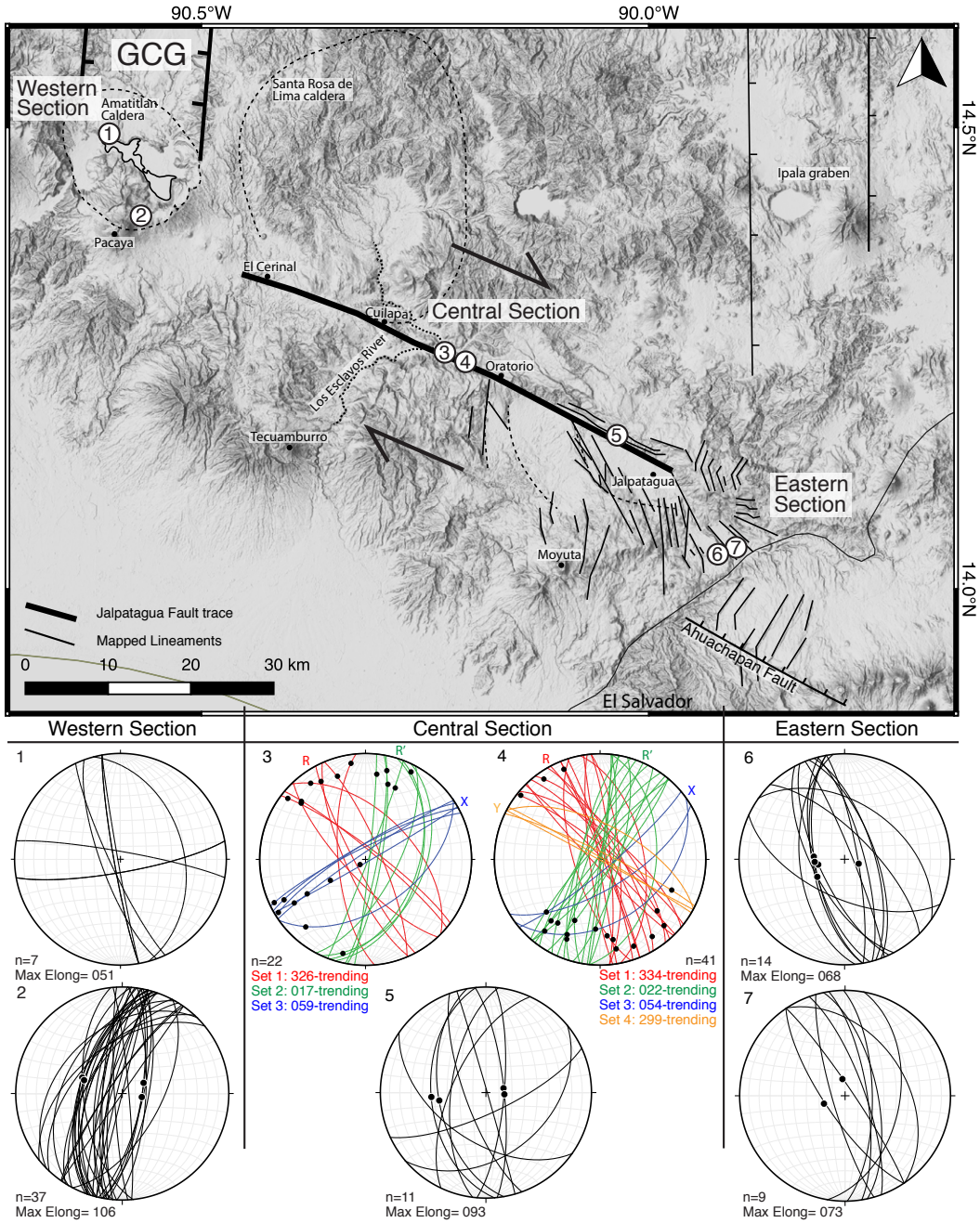

Figure 2. A 20 m digital elevation model (OpenStreetMap contributors, 2015) of southeastern Guatemala showing major structures and lineaments and locations of faulted outcrops. Data were collected within three study areas along and near the Jalpatagua fault: western, central, and eastern sections. Fault data collected from each location are displayed below the map. GCG—Guatemala City graben.

TABLE 1. DESCRIPTIONS AND PUMICE MINERALOGY OF COLLECTED SAMPLES

Sample	Unit description	Additional descriptions	Present structures
17JF23a Location 1	8–10-m-thick, white pumice–rich lapilli tephra containing mostly pumice fragments (centimeters to tens of centimeters long), phenocrysts, and ash. Unit has a granular appearance due to the abundance of pumice fragments. Unit is poorly indurated and easily eroded by wind. Interpreted as E tephra from Amatitlan caldera.	Pumice mineralogy: Pumice contains 73% glass, 4% mafic phenocrysts, and 23% felsic phenocrysts. Mafic phenocrysts are dominantly biotite, with lesser amounts of hornblende, and trace hypersthene. Magnetite makes up 12% of the mafic phenocrysts. Pumice vesicles range from frothy to linear within pumice fragments.	N-S–trending normal faults
17JF23b Location 1	2–6-m-thick, white pumice–rich lapilli tephra containing pumice fragments (centimeters long) of similar shape and size, along with phenocrysts and ash. Pumice fragments are smaller and less abundant than those in unit 17JF23a. Interpreted as C tephra from Amatitlan caldera.	Pumice mineralogy: Pumice contains 86% glass, 5% mafic phenocrysts, and 9% felsic phenocrysts. Mafic phenocrysts are dominantly hornblende with trace amounts of hypersthene, with magnetite being 38% of the mafic phenocrysts.	Normal faults
17JF26 Amatitlan caldera	Tan, coarse-grained granite with highly weathered biotite crystals. Much of the tan color comes from oxidation surrounding biotite crystals.	Thin section: Large quartz and plagioclase crystals with deteriorated biotite crystals. $^{40}Ar/^{39}Ar$ age of 7.43 ± 0.43 Ma	
17JF65 Location 3	Crystal-rich welded tuff. White, highly indurated welded tuff with plagioclase and mafic crystals and aphanitic groundmass. Reduced to powder in highly faulted areas containing epidote in fault gouge.	Thin section: Very fine-grained groundmass of quartz showing signs of healing, no vesicles visible, few plagioclase and mafic crystals.	NW-striking and NE-striking strike-slip faults
14JF2 Location 4	Highly weathered gray, biotite-rich granite. Granite has a granular appearance as it crumbles easily in the hand to gravel-sized grus. Biotite fragments are relatively small and weathered, but abundant.	Too weathered to create a thin section. $^{40}Ar/^{39}Ar$ age of 10.15 ± 0.04 Ma	Strike-slip faults ranging from NW-N-NE-striking
WH19S1 Location 7	Lower tephra; ~3.3-m-thick, light-colored pumice-rich lapilli tephra containing light-gray pumice fragments (0.5–16 cm long), with occasional dark-gray pumice fragments (17–36 cm long), 25% ash matrix and 3%–4% small, angular basalt lithics. Pumice fragments are highly vesiculated. Tephra is poorly indurated. At the base of the tephra, there is a 50–70 cm layer of basaltic lithics (2.5–13 cm) with upward grading into the tephra.		NW-striking normal faults
WH19S2 Location 7	Upper tephra; 4.9-m-thick, light-colored tephra with similar gray pumice to the lower tephra (0.5–6 cm long), lack of dark-gray pumice, 50%–60% matrix, and very few lithics. Tephra is poorly indurated and erodes easily.		NW-striking normal faults

southern Guatemala. Detailed descriptions of individual eruptions often include isopach maps and suggested sources (Koch and McLean, 1975; Rose et al., 1999). Quaternary silicic tephras are typically identified as very white or light colored and poorly indurated, while Neogene tephra deposits are darker in color and well indurated. This distinction aids in a first-order identification in the field, which can be followed by a comparison to the major Quaternary tephras or Neogene formations. Figure 3, modified from Rose et al. (1999), displays the spatial and temporal record of the major Quaternary tephras across south-central and southeastern Guatemala. Smaller-volume Quaternary tephras, lavas, and reworked deposits from individual volcanic centers also exist in southern Guatemala, which complicate unit identification. In some cases, geologic studies have been conducted on smaller volcanic sources south of the Jalpatagua fault, which aided unit identification at our outcrops (Bethancourt et al., 1976; Duffield et al., 1992). However, detailed stratigraphy is generally absent from southeastern Guatemala.

In general, the Neogene rocks of southeastern Guatemala—adjacent to the Jalpatagua fault—are composed of granites, rhyolitic, andesitic, and basaltic tephras and lavas, and reworked sediments (Reynolds, 1977, 1980, 1987). Individual eruptions or events are not defined as they are for the Quaternary tephras. Instead, three bulk formations have been established for Neogene deposits across this region of Central America (Fig. 3): (1) the upper Cuscatlán formation (Pliocene); (2) the middle Básalmo formation (only present south of the volcanic arc, approximately Upper Miocene to Pliocene); and (3) the lower Chalatenango formation (Middle to Upper Miocene; Reynolds, 1977, 1980, 1987). Formation names follow the nomenclature established for El Salvador, as adopted by Reynolds (1980, 1987) and established by Wiesemann (1975).

GEOLOGIC AND GEODETIC DATA

Geologic Data

The Jalpatagua fault has a clear fault trace across southeastern Guatemala, which was identified on photos or digital elevation models (DEMs) and was the focus of prior geomorphic studies. However, with the tropical, vegetated environment in Guatemala, no outcrops of the fault zone are reported in the literature or were found during our field work. Therefore, we relied on analysis of minor faulting, often called secondary faulting, collected in road outcrops and quarry exposures adjacent to the Jalpatagua fault trace to understand the finer details of movement and deformation along the fault trace. Fault data were collected in three areas: (1) central section: multiple sites along the Jalpatagua fault trace (locations 3, 4, and 5; Figs. 2 and 4); (2) eastern section: near the Guatemala–El

Salvador border (to characterize faulting near the eastern termination; locations 6 and 7; Figs. 2 and 4); and (3) western section: within the Amatitlan caldera (to characterize faulting near the western termination; locations 1 and 2; Figs. 2 and 4). At each outcrop, structural data (fault orientations, lineations, bedding orientations, and outcrop transect length) were collected along with rock samples for unit correlation and age dating.

Observations of Secondary Faulting

Central section. Data were collected from three outcrops along the Jalpatagua fault trace: Strike-slip faulting was observed in quarries at locations 3 and 4; and normal faulting was observed within a road cut at location 5 (Figs. 2 and 4). Quarrying activity at locations 3 and 4 within the central section provided exposed horizontal surfaces, which allowed us to directly recognize strike-slip faulting.

Minor strike-slip faults ($n = 79$) were observed in two lithologies: (1) a white, welded tuff at location 3; and (2) a coarse-grained Miocene granite at location 4 (Table 1). The welded tuff of location 3 most closely correlates to a similarly described Miocene welded tuff of the Chalatenango formation (Fig. 4; Reynolds, 1987). The coarse-grained granite of location 4 contains large biotite crystals, is highly weathered, and is pervasively cataclastically shattered, consistent with its location <1 km from the Jalpatagua fault. Additionally, at least two basalt dikes crosscut the granite, providing offset markers for only two faults (Fig. 4). A sample of the granite was collected for $^{40}Ar/^{39}Ar$ dating analysis (sample 14JF2).

Strike-slip faults measured at locations 3 and 4 have a large variation of orientations but can be separated into four subsets, which correlate to minor fault arrays commonly observed in field-based and experimental studies (Fig. 2; Tchalenko, 1970; Logan et al., 1979):

Set 1: average 330°-oriented strike-slip faults (~35° clockwise from Jalpatagua fault trace orientation) with slickenline rakes of ~10° from the NW and SE (similar to R shears; red planes in Fig. 2);

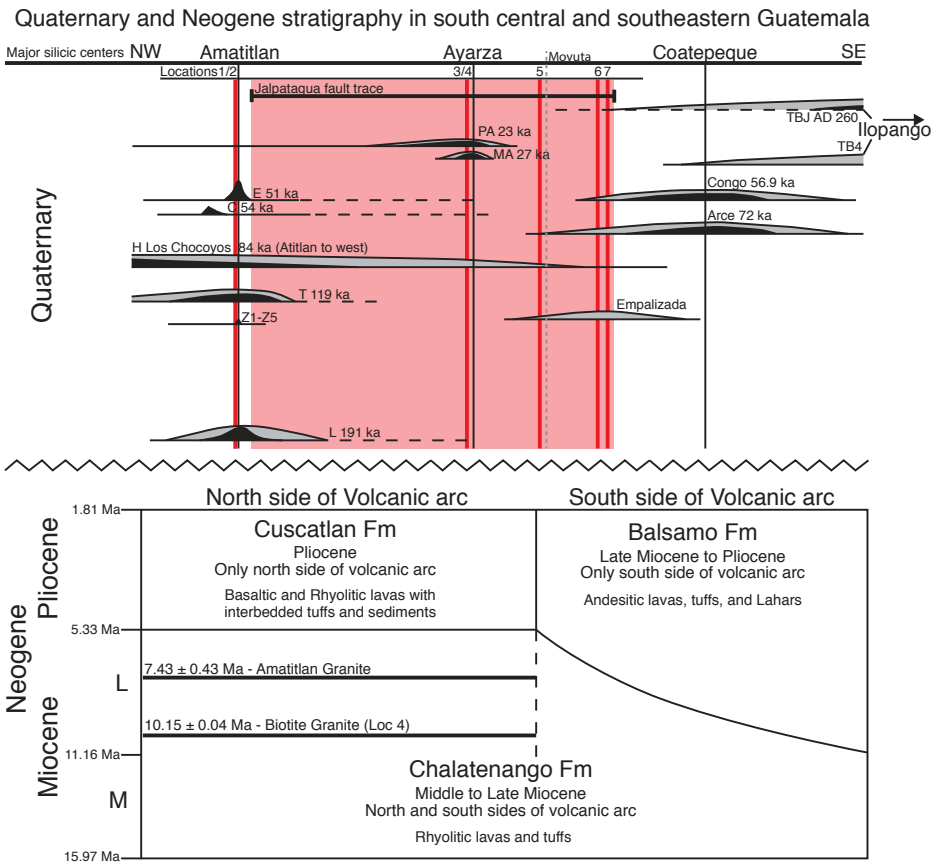

Figure 3. Quaternary and Neogene stratigraphy of south-central and southeastern Guatemala. Top portion describes the Quaternary stratigraphy (modified from Rose et al., 1999), with vertical red lines indicating the locations of outcrops in relation to the major rhyolitic centers. The larger red-shaded box outlines the area covered by the Jalpatagua fault trace. Bottom portion describes the Neogene stratigraphy (M—middle, L—late) and displays the two $^{40}Ar/^{39}Ar$ dates reported in this paper.

Set 2: ~020°-oriented strike-slip faults (~85° clockwise from Jalpatagua fault) with slickenline rakes of ~20° from NE and SW (similar to R′ shears; green planes in Fig. 2);

Set 3: ~055°-oriented strike-slip faults (~60° counterclockwise from Jalpatagua fault orientation) with rakes of ~15° from SW (X shears, nearly perpendicular to P shears; blue planes in Fig. 2); and

Set 4: faults with an average orientation of ~300°, subparallel to the Jalpatagua fault (or Y-shears; yellow planes in Fig. 2).

We could not determine the sense of motion for each strike-slip fault, but field observations, and the expected motion of secondary faults based on the Riedel shear model, suggest right-lateral motion along set 1 and set 4 (Jalpatagua-parallel) faults,

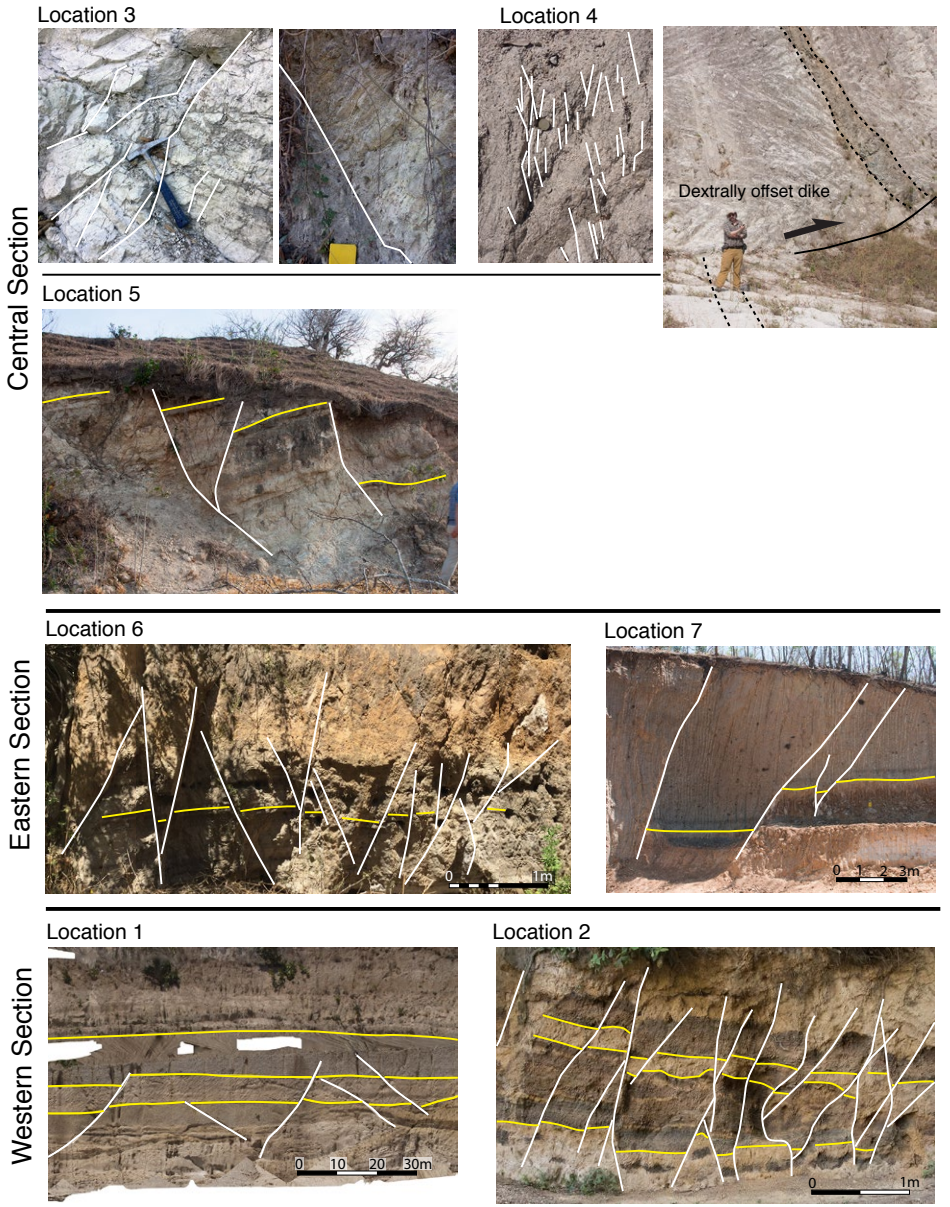

Figure 4. Annotated outcrop photos from faulted outcrops documented in the three study sections. White lines trace faults, and yellow lines identify marker horizons. For location 3 and 4 photos, left photos display strike-slip faults, while right photos show faults that indicate measurable offset. Remaining outcrop photos all document normal faulting.

and left-lateral motion along set 2 and set 3 faults (Fig. 5; Tchalenko, 1970; Logan et al., 1979).

We could only determine offset amounts for two strike-slip faults within the biotite granite quarry that offset a single, roughly subvertical basaltic dike (location 4; Fig. 4). The first fault zone is oriented nearly parallel to the Jalpatagua fault (~300°) and dextrally offsets the dike by 6 m, and the second fault zone is oriented ~320°, with 7.5 m of dextral offset. The exposure of the quarry bottom allowed the direct observation of fault offsets.

Normal faults were measured at the final outcrop within the central section at location 5, within a white, loose ash to the north of the Jalpatagua fault scarp (Figs. 2 and 4). The color and nonindurated nature of the deposit suggest a Quaternary age for the layered deposit, but a more precise tephra identification could not be made. Normal faults have an average N-S orientation (n = 11), with tens of centimeters of normal offset, and the few observable slickensides (n = 4) indicated downdip movement (Fig. 5). All measured normal faults continue into the soil horizon to the surface.

Eastern section. In the eastern section, normal faults were observed at two outcrops southeast of the Jalpatagua fault termination and ~1.8 km from the El Salvador border (locations 6 and 7; Figs. 2 and 4). Faults were measured in two different lithologies: (1) highly indurated, thinly bedded ash and reworked ash deposits at location 6, most likely part of the waterlain sediments of the Neogene Cuscatlán formation (Reynolds, 1987); and (2) loose, white and gray tephra deposits at location 7, containing mafic lithics and pumice, in a flat valley less than 2 km NE of location 6. The tephra deposits of location 7 do not correlate to any of the major Quaternary ashes, based on location and thickness of depositions; therefore, two tephra samples were collected at location 7 to correlate to the known stratigraphy (Table 1; samples WH19S1 and WH19S2). Normal faults strike NW, with centimeters to meters of normal offset (location 6: n = 13; location 7: n = 9; Figs. 2 and 4). Slickenlines with pitches ranging from 78° to 88° were observed on a few fault planes at each outcrop (location 6: n = 5; location 7: n = 2), indicating downdip movement. At both outcrops, faults reach the surface.

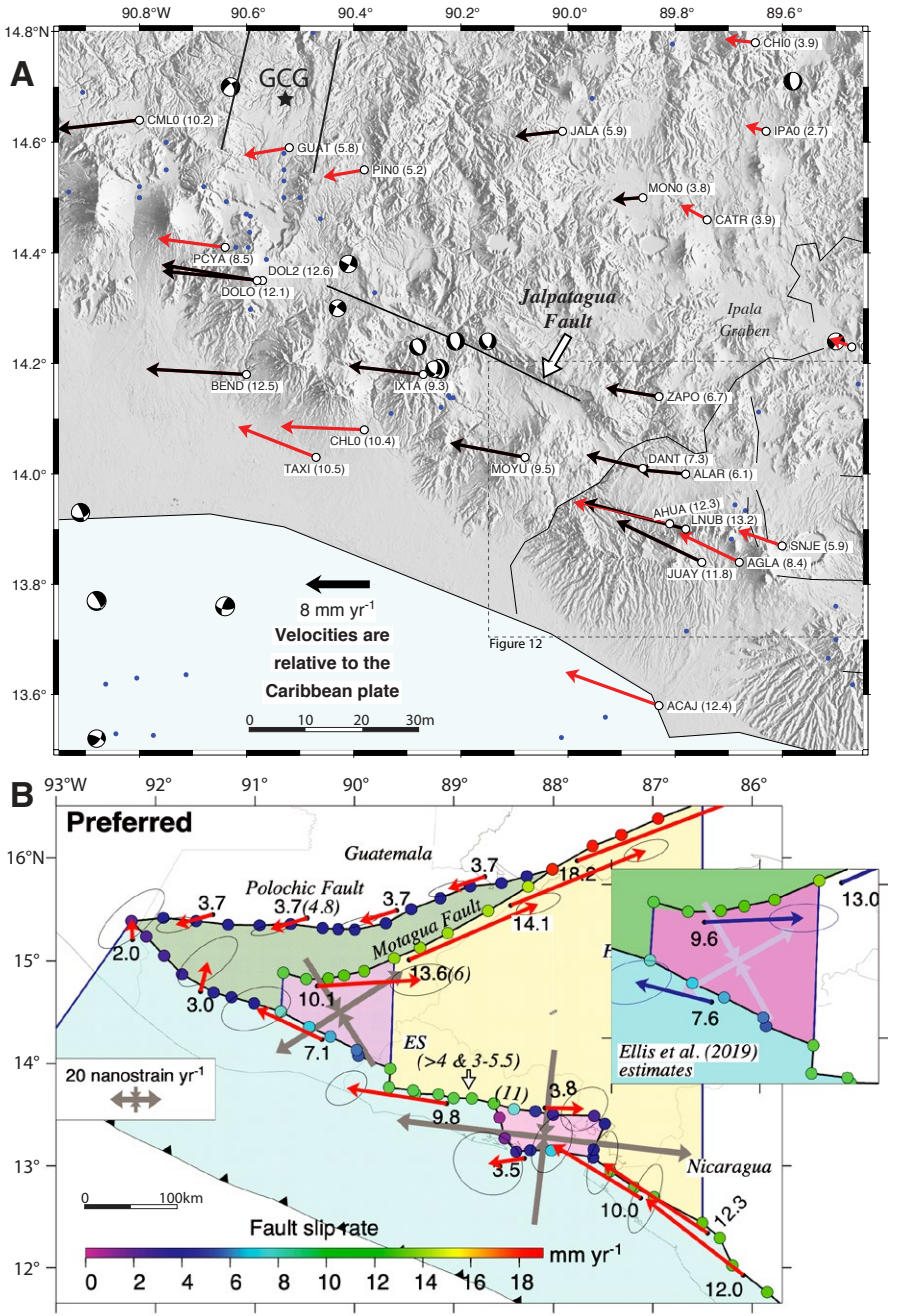

Figure 5. (A) Velocities of global positioning system (GPS) sites in mm yr^{-1} near the Jalpatagua fault with respect to a stationary Caribbean plate and corrected for time-dependent effects associated with large regional earthquakes in 2009 and 2012 (see text). Sites with red arrows have velocities that were derived using the same GPS data as in Ellis et al. (2018, 2019). Sites with black arrows have velocities that incorporate all the data from Ellis et al. (2018, 2019) and additional observations described in the text. (B) Estimates of fault slip rates in mm yr^{-1} and deforming block strain rate magnitudes and principal axis orientations for an elastic block model updated from Ellis et al. (2019) using the Ellis et al. 200+ station GPS velocity field and new GPS data described herein. Slip rates at the strike-slip fault nodes are color coded according to the color scale on the map. Each red arrow and its adjacent number specify the velocity that is estimated for the plate or block on which the arrow originates with respect to the plate or block located on the other side of the adjacent block-bounding fault. The fault slip velocities and strain rates predicted by the Ellis et al. (2019) model are shown for comparison in the inset map. The shaded regions define the five elastic blocks for which rotation and deformation parameters were estimated in our inversion (see text). GCG—Guatemala City graben; ES—El Salvador. Figure is modified from Ellis et al. (2019).

Additional isolated NW-striking faults were found within this area.

Western section. Two faulted outcrops were studied within the Amatitlan caldera to determine if any evidence of Jalpatagua-related faulting could be observed west of the fault trace. Outcrops are located on the north (location 1) and south (location 2) sides of the caldera (Fig. 2). Field work identified no other faulted features past the western termination of the Jalpatagua fault trace or on the eastern slope of Pacaya volcano.

In general, the stratigraphy and faulting are very different between the two western section outcrops. On the north side of the caldera (location 1), normal faults ($n = 9$) strike E and NNW with meters of normal offset and occur in thick Amatitlan tephra deposits (Figs. 2 and 4). No recorded fault planes had observable slickenlines. Within the tephra deposits, we observed possibly three stages of normal faulting, as faulted lithologies are capped by younger deposits with additional faults or younger unfaulted deposits. Samples were collected to correlate to the known stratigraphy to constrain fault timing (samples 17JF23a and 17JF23b).

On the south side of the caldera (location 2), the stratigraphy is dominated by volcanic flows and more recent activity related to the Pacaya volcano (Fig. 4). Numerous NNW-oriented normal faults ($n = 33$), with centimeters to tens of centimeters of normal offset, cut a thinly layered deposit of scoria, pumice, and ash, most likely from small eruptive events from Pacaya volcano (Figs. 2 and 4). A few fault planes with observable slickenlines ($n = 4$, pitches between 80° and 90°) indicate downdip movement. In addition, the faulted outcrop is overlain by an unfaulted, white pyroclastic flow, which was sampled to constrain fault timing (sample 17JF13).

Lineaments

Besides the secondary faulting observed in quarries and road cuts, a set of NW-trending lineaments is present southeast of the eastern termination of the Jalpatagua fault near the El Salvador border (Fig. 2; mapped on the 20 m DEM of Guatemala; OpenStreetMap contributors, 2015). We suggest that the lineaments represent faults, since many of the lineaments were mapped and identified by previous workers in the 1960s and 1970s using aerial photos (Williams, 1960; Carr, 1974). Additionally, many of the lineaments likely represent normal faults, as transects show the presence of asymmetric hills, suggesting a fault scarp and tilted fault block, and downward movement of a hanging wall typically toward the direction of the Jalpatagua fault (Fig. 5). The mapped lineaments in Figure 2 range in orientation from 132° to 181° with lengths from 0.5 km to nearly 10 km, with a peak trend at ~155°.

Geodetic Data

Prior to this work, the most recent estimate of the Jalpatagua fault slip rate was based on an inversion of more than 200 GPS site velocities on seven blocks or plates in northern Central America and southern Mexico to estimate their relative motions, their internal deformation, and slip velocities and interseismic locking for the faults that separate the blocks (Ellis et al., 2019). Relevant to this study, most of the GPS site velocities in southern Guatemala were estimated from only two occupations spanning a 2.0 yr period. For this study, we incorporated new GPS data that we collected at 10 preexisting stations and three new stations (ALAR, DANT, and JUAY in Fig. 5A) in western El Salvador and southern Guatemala (locations and velocities given by the black arrows in Fig. 5A). The new data extend the time series at all the GPS sites in our study area to at least 5 yr and include sites in western El Salvador that are well located for constraining the eastern termination of the Jalpatagua fault.

METHODS

Fault System Structural Analysis

Fault Slip Assumptions

The following paleostress and strain methods heavily relied on the assumption that our observed normal faults have true downdip movement and reliable fault slip data. While we observed slickenlines on only 20% of fault planes, the pitches were always greater than 78°, and a large majority centered around 88°. Therefore, we only observed evidence of nearly true downdip motion for faults with normal offsets, and we extended this observation to faults without any observable slickenlines. The greatest uncertainly lies with location 1, where no slickenlines were observed; however, we still extended the assumption of downdip motion.

Paleostress

Paleostress orientations were estimated from fault slip data collected at the two strike-slip–dominated outcrops along the Jalpatagua fault (locations 3 and 4; central section), and three normal-fault–dominated outcrops along the Jalpatagua fault and near the eastern termination (location 5, central section; locations 6 and 7, eastern section). The paleostress inversion software Fault and Stress Analysis (FSA; Célérier, 2018) was used to determine the reduced stress tensors that best fit the given data.

Paleostress inversion methods estimate principal stress orientations with given fault slip data. This analysis is done by calculating the reduced stress tensor, which has four unknowns: the orientations of the three principal stress axes σ1, σ2, and σ3 (where $\sigma1 > \sigma2 > \sigma3$) and R, the aspect ratio, which represents the shape of the stress ellipsoid ($R = [\sigma1 - \sigma2]/[\sigma1 - \sigma3]$; Célérier, 1988; Célérier et al., 2012). Multiple assumptions must be met for a stress inversion analysis to be valid (e.g., Carey, 1976; Etchecopar et al., 1981; Angelier et al., 1982; Michael, 1984; Angelier, 1984, 1994): (1) Faults occur in an isotropic medium; (2) the stress state is homogeneous, no torque is present, and it can be described by a symmetric stress tensor; and (3) slip on faults is parallel to the resolved shear stress on the fault plane. Common criticisms of the dynamic analysis of fault slip data include: (1) Fault slip data better describe strain rather than paleostress; and (2) the stress field is perturbed near major

faults and by fault interactions (e.g., Marrett and Allmendinger, 1990; Twiss and Unruh, 1998; Gapais et al., 2000; Žalohar and Vrabec, 2008; Kaven et al., 2011; Lejri et al., 2015; Riller et al., 2017). However, paleostress data are useful for comparison between different areas and to check consistency with the present-day (only two-dimensional [2-D]) strain rate tensor derived from GPS.

To determine best-fitting paleostress tensors for a given fault slip data set, the FSA program uses a random search method to generate a particular number of reduced stress tensors (Etchecopar et al., 1981). For each generated stress tensor, predicted slickenlines are calculated for each given fault, which represent the direction of slip that would occur on the fault given the particular stress tensor (Wallace, 1951; Bott, 1959). Misfit angles are calculated between the predicted and real slip data, and this information is used to determine how well a reduced stress tensor represents the data. For normal fault data sets (locations 5, 6, and 7), the assumption of downdip motion was used to generate slip vectors for the fault planes with no observable slickenlines. The program reports the best-fitting stress tensors based on the lowest collective misfit angles. Additional examples of methods and application of FSA can be found in Burg et al. (2005) and Garibaldi et al. (2016).

For the FSA of fault slip data from locations 3, 4, and 5, 10,000 stress tensors were randomly generated and compared to each data set. Of the 10,000 random stress tensors, the best 50 were retrieved and plotted on a stereonet to determine the mean and variance of the stress orientations that would best represent the given data. The top 50 were used because this number of points showed a clear main cluster with visible variance, yet the variance was not large enough to cause the mean to deviate from the main cluster. For each location, all fault slip data were initially analyzed in the FSA program, but faults that consistently produced large misfit angles (typically greater than 30°) for the top five stress tensors were removed, and the analysis was rerun. Data removal resulted in two faults being removed for location 3, four faults removed for location 4, and no faults removed from location 5. Figure 6 contains contoured stereonet plots of the

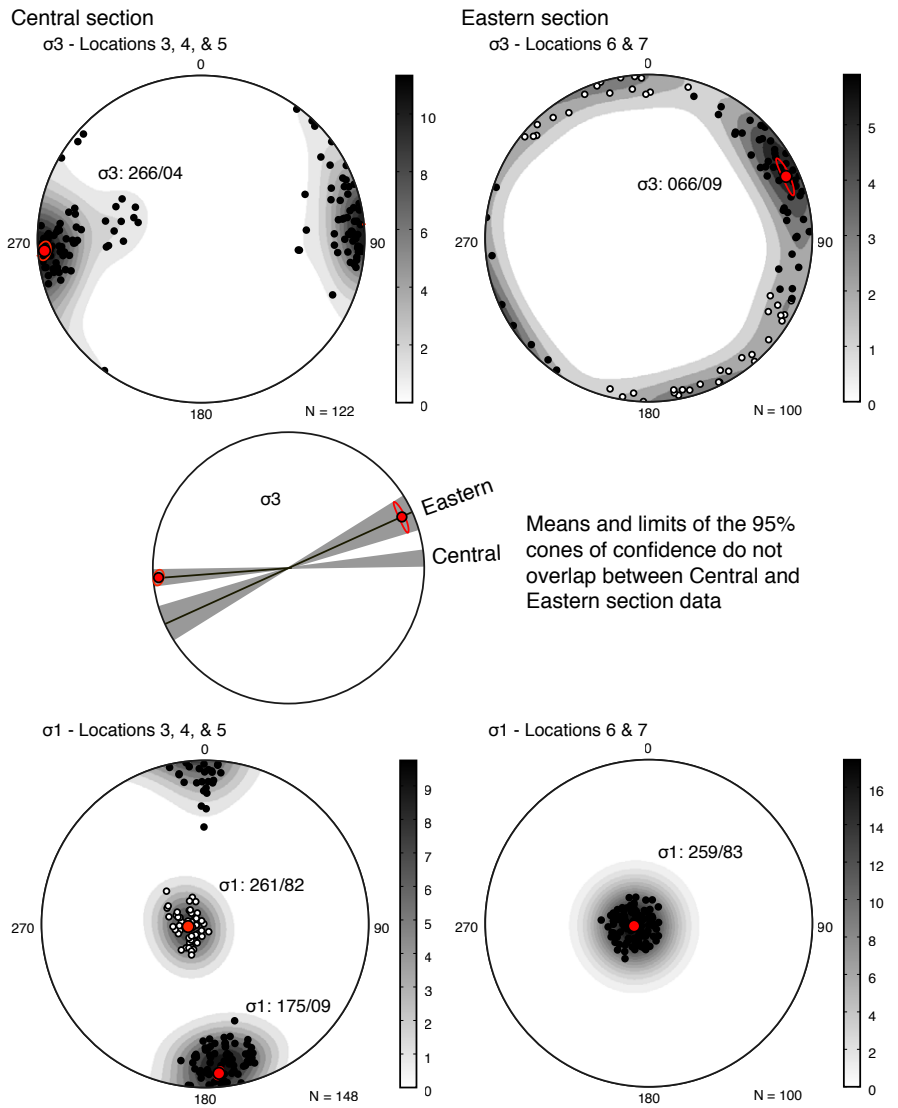

Figure 6. σ3 and σ1 orientation results from fault and stress analysis (FSA) of central (left side of figure) and eastern (right side of figure) section fault slip data. Individual data points are plotted as dots, with 1σ Kamb contouring applied. Black and white dots for location 6 and 7 σ3 data represent the main cluster used to calculate the eigenvector and cone of confidence (black) and the remaining data (white). For location 3, 4, and 5 σ1 data, black dots represent σ1 data from strike-slip faults, and white dots represent σ1 data from normal faults. The maximum eigenvector for each data set, or cluster, is identified by a red dot, with a red ellipse signifying the 95% cone of confidence (many cones are too small to be seen on the figure). In the middle of the figure, a rose diagram indicates the mean and cone of confidence limits for central and eastern section σ3 data.

combined resulting σ3 orientations (maximum elongation) and σ1 (maximum compression) for all three locations. Modified Kamb contouring was applied with 1σ contours, which indicated that each data set had clear clusters of points that were significantly different from a data set of random orientations. Outliers were removed from each data set to preserve the calculated mean of the main cluster, then eigenvectors were calculated to find the mean of each data cluster, and the 95% confidence cone was calculated using the Bingham statistical model. Contouring and statistics were all done in software program Orient, which provides statistics and plotting features (Vollmer, 1995, 2015). The same method outlined in the this section was applied to FSA analyses of normal fault slip data from locations 6 and 7 (Fig. 6). No faults were removed from either data set.

Strain

Maximum elongation direction. One-dimensional strain was estimated for each of the five normal-fault–dominated outcrops observed in the central, eastern, and western sections (excluding locations 3 and 4, which lacked markers to record offset). At each outcrop, normal faults (orientations and fault separations on the outcrop face) were recorded along a transect of measured length that started and ended at a fault. The orientations of marker beds were also recorded along with any visible slickenlines on fault plane surfaces (20% of fault planes). For each transect, all faults were used to calculate the direction of maximum elongation (Figs. 2 and 7). Titus et al. (2007) found that the direction of maximum elongation for dominantly dip-slip faults is the orientation with the highest ratio between apparent heave, h_{app}, and total heave, h_{tot}, for all faults in a given population. Plotting the h_{app}/h_{tot} ratio by azimuth provides a graphical method to determine maximum elongation, and it allows comparison of various fault samples simultaneously or analysis of any abnormalities within a data set (Fig. 7). The azimuth with the highest value (meaning that the apparent heave is closest to the total heave) represents the maximum elongation direction for a given transect/fault population. Table 2 and Figure 8 illustrate the variation of maximum elongation directions among outcrop locations.

Elongation estimate. To estimate elongation for each transect, two sets of calculations were completed: (1) offsets from observable faults (elongation); and (2) offsets derived from observable faults and unobservable faults using power-law

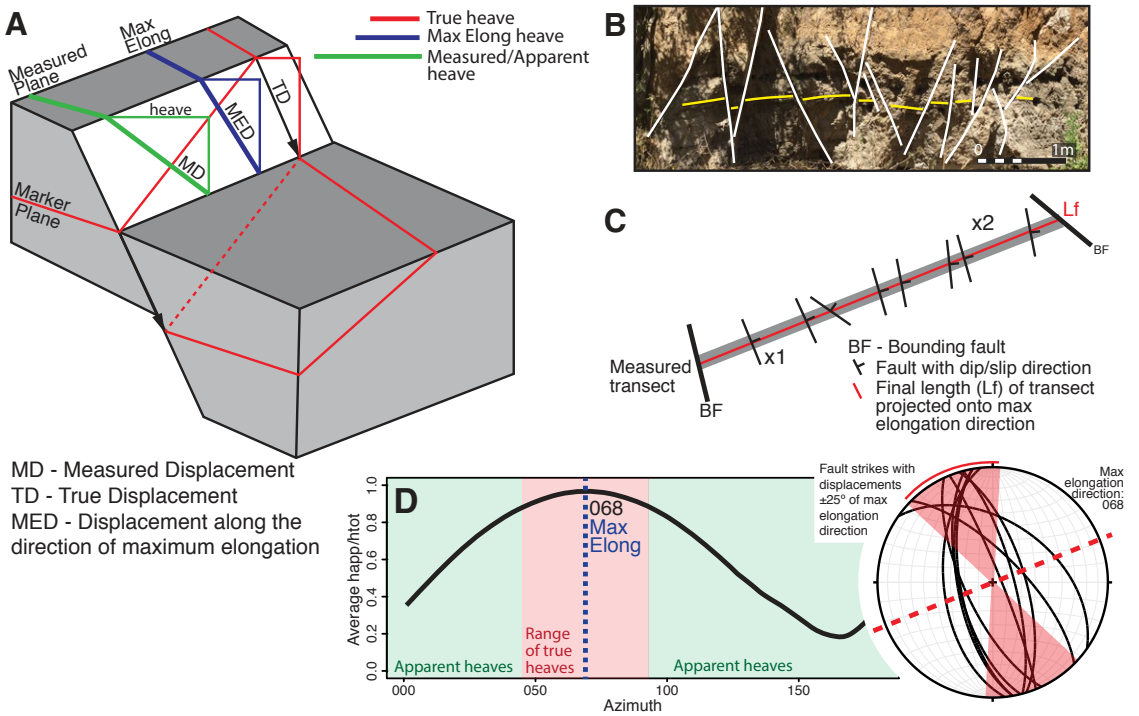

Figure 7. Method for estimating elongation. (A) Block diagram demonstrating the geometric difference between true displacement and heave along a fault (TD in red), the measured displacement and heave along an outcrop face (MD in green), and the displacement or heave along the estimated direction of maximum elongation (MED in blue). Figure is based on figure 1 in Xu et al. (2009). (B) Annotated outcrop photo of normal faults measured at location 6. (C) Map-view schematic of location 6 transect B used to determine elongation. (D) Apparent heave/total heave (happ/htot) chart from location 6 data, indicating a maximum elongation direction of 068°. Green-shaded regions show the portions of the curve that represent apparent heaves. The red-shaded portion indicates the range of azimuths where true heaves were observed. The blue dashed line is the maximum elongation orientation. To the right of the chart, stereonet of location 6 data with a 50° red-shaded window centered on the 068° maximum elongation direction shows which data were used in the elongation estimation. Only one datum falls outside of the threshold and, therefore, was excluded from the elongation estimation.

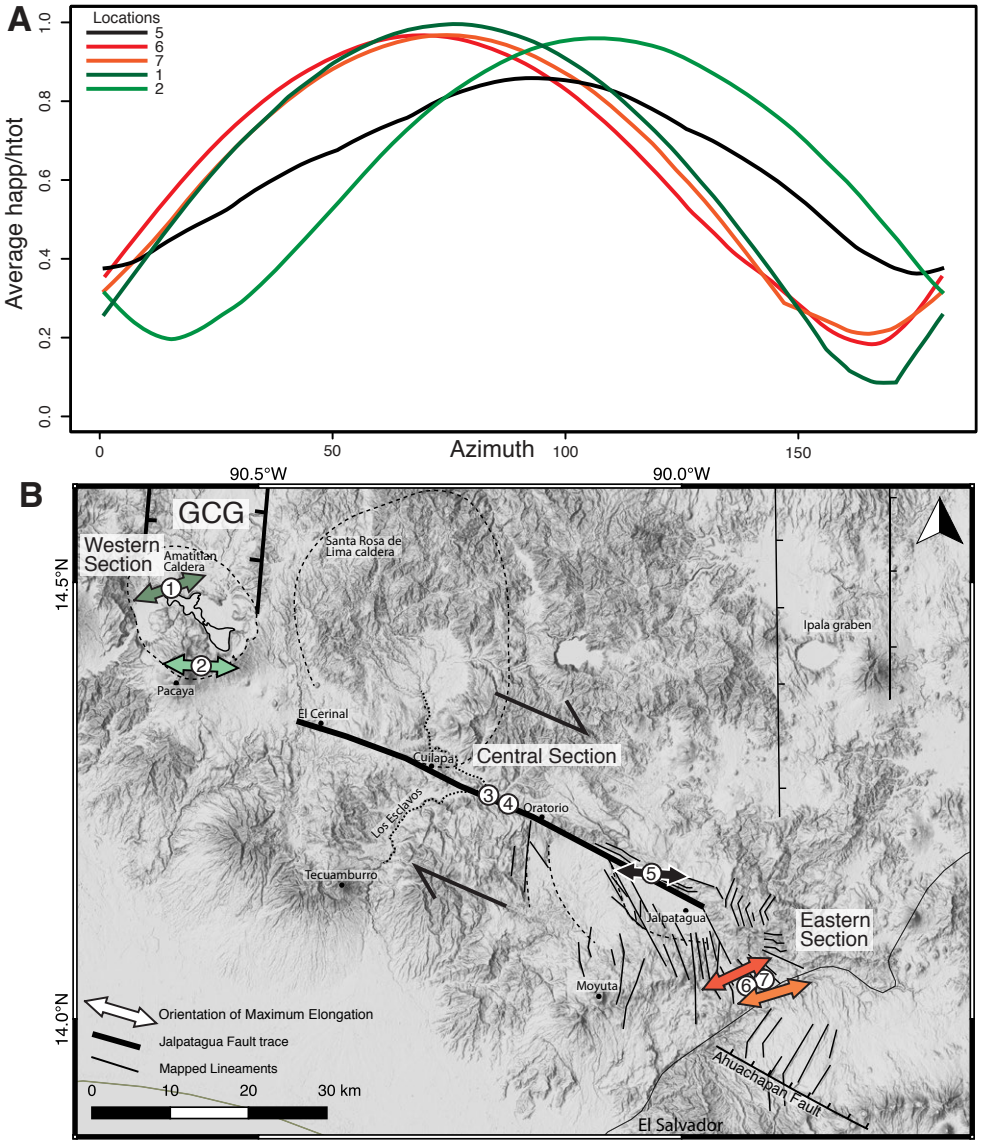

Figure 8. (A) Graphical method to determine the direction of maximum elongation for each normal fault sample. The *y* axis displays the average ratio of apparent heave (h_{app}) to total heave (h_{tot}) for each azimuth (*x* axis, 0°–180°). Locations related to the Amatitlan caldera are shades of green (locations 1 and 2), location 5 along the Jalpatagua fault is black), and Guatemala–El Salvador locations (locations 6 and 7) are shades of red/orange. (B) 20 m digital elevation model of southeastern Guatemala with colored arrows indicating the directions of maximum elongation estimated for each normal-fault–dominated outcrop. Color coding matches that of panel A. GCG—Guatemala City graben.

relations (e.g., Scholz and Aviles, 1986; Walsh and Watterson, 1992; Marrett and Allmendinger, 1991, 1992; Gross and Engelder, 1995). To estimate the elongation from observable faults, the true displacement of each fault was first calculated following the method outlined in Xu et al. (2009), since initial fault measurements from outcrop faces actually represent apparent offsets (green heave in Fig. 7A). For this method, fault orientation, marker bed/unit orientation, slickenline pitch, and transect orientation must all be specified. To reiterate, down-dip slip (rake of 90°) was assumed for moderately (30°–70°) dipping normal faults where slickenlines were not visible but where normal offset and slip sense were observed on other faults within the same outcrop. With true displacement calculated in this manner, the true horizontal displacement component (heave) was determined for each fault (red heave in Fig. 7A).

True horizontal displacements were estimated for all faults within ±25° of the maximum elongation direction, which maximizes components of heave parallel to the elongation direction (Fig. 7). To ensure unbiased elongation calculations, the offsets/heaves from bounding faults were not used in elongation calculations. Finally, each true horizontal heave value was projected onto the maximum elongation direction (blue heave in Fig. 7A). Projected heave values were summed to determine the change in length (ΔL) for each traverse. The measured length of each transect was also projected onto the maximum elongation direction for each traverse (L_f). Elongation for each transect was calculated as follows:

$$e = (L_f / L_f - \Delta L) - 1, \quad (1)$$

where e is elongation, L_f is the final length of each traverse projected onto the maximum elongation direction, and ΔL is the change in horizontal length (the sum of all fault heaves used in the calculation) in the maximum elongation direction. Elongations for all transects, as well all L_f and ΔL values, are included in Table 2.

Revised elongation. Previous research has shown that small faults and small offsets can greatly affect elongation measurements, up to 60%

TABLE 2. MINOR FAULT ANALYSIS RESULTS

Location	*Lf* (m)	Maximum elongation (azimuth)	No. of faults	Δ*L* (m)	Elongation (%)	h_e (m)	Δ*Lr* (m)	Revised elongation (%)
Amatitlan caldera								
1	221.0	075	6	1.3	0.6	–	–	–
2	11.0	106	38	1.6	17.3	1.7	3.3	43.5
Jalpatagua fault								
5	12.8	093	11	1.7	15.4	0.2	1.9	17.8
Guatemala–El Salvador border								
6	4.6	068	9	0.3	7.2	–	–	–
7	15.5	073	6	2.2	16.2	1.7	3.8	33.0

Notes: Dash indicates calculations could not be made for revised elongation. *Lf*—final length of transect; Δ*L*—change in transect length; h_e—amount of horizontal displacement (heave) due to movement on small faults; Δ*Lr*—revised change in transect length.

in some studies (Marrett and Allmendinger, 1991, 1992; Walsh et al., 1991). Therefore, revised elongation estimates were also calculated to include the contribution of small faults with unobservable, yet significant offsets, following the methods outlined by Gross and Engelder (1995). Fault populations were plotted as the log of cumulative frequency (where 1 is the largest displacement, and *n* is the smallest displacement) versus the log of each corresponding displacement. If the fault population follows a fractal fault geometry, faults with intermediate displacements will show a linear relationship on frequency-displacement plots (Fig. 9). The ends of the frequency-displacement plot typically do not show a linear relationship because small faults and large faults are often undersampled. A line can be fitted to the linear portion of the frequency-displacement plot (Fig. 9), and the value of the slope (–C) is then used to compute the horizontal displacement due to small faults (h_e) using the equation:

$$h_e = h_N \frac{C}{1-C}(N+1)\left(\frac{N}{N+1}\right)^{\frac{1}{C}} \quad (2)$$

where h_N is the smallest displacement used to calculate the slope, and *N* is the number of faults used in the regression. Frequency-displacement plots with regression lines for all five outcrops are shown in Figure 9. This equation only works when $C > 1$. A revised Δ*L* was calculated by adding h_e to the previously calculated Δ*L*, with the result being the revised elongation. The revised elongations, along with the calculated h_e and revised Δ*L* values, are also included in Table 2. Revised elongations were not completed for those transects that contained too few faults to confidently determine the value of *C*. In these cases, the calculated elongations reflect a minimum elongation value.

Lineaments

Maximum elongation direction and elongation amounts were estimated for the lineaments identified near the eastern termination of the Jalpatagua fault. Authemayou et al. (2011) estimated elongation on lineaments in western Guatemala using a paleosurface to estimate fault displacement based on an assumed 50°–80° normal fault dip. However, this approach was not possible within our field area due to the absence of a reliable paleosurface. Therefore, we applied a similar process, with additional assumptions, to estimate elongation along three lineament transects that best displayed an occurrence of normal faulting. The locations of the three transects are presented in Figure 10 along with the topographic profiles, which were created using a 20 m DEM (OpenStreetMap contributors, 2015). Based on the topographic profiles and previous observations of downdip movement on normal faults in this area, we assumed that these lineaments represented normal faults with true downdip movement. A transect orientation of 067° was determined by calculating the maximum elongation orientation for all lineaments used in the three transects. With the absence of a paleosurface, the current topography was used as an offset marker by determining the general dip between faults (Fig. 10). Similar to Authemayou et al. (2011), fault dips of 50° and 80° were used to calculate end-member offsets and elongation estimates. Last, to calculate a final length for elongation estimates using the same method as above for minor faults, an average fault spacing was calculated for each transect, and the distance was added to the first and final faults. The purpose of this step was to create synthetic bounding faults that allowed the use of all lineaments for the elongation estimation.

Geochemistry

Geochemistry was used to correlate units to the known stratigraphy. Major- and trace-element geochemistry of seven samples was obtained by X-ray fluorescence (XRF) analysis (conducted by the Geoanalytical Laboratory at Washington State University; Table 3A). Unit correlation was only applicable for the two tephra samples collected from location 1 (17JF23a and 17JF23b), since the samples were located within the documented area of Quaternary tephra deposition. Similarity coefficients were calculated between the two tephras and 10 Quaternary tephras that had documented geochemistry in the literature to aid in unit correlation (Table 3B; Borchardt and Harward, 1971; Wunderman and Rose, 1984; Rose et al., 1987; Sarna-Wojcicki et al., 1984; Sarna-Wojcicki, 2000). Similarity coefficients were calculated using the normalized weight percent of the following major elements: SiO_2, FeO, TiO_2, Al_2O_3, MgO, CaO, Na_2O, K_2O, and P_2O_5; and parts per million of the following trace elements: Sc, Ba, Rb, Sr, Zr, and La. Based on geochemistry data alone, sample 17JF23a was most similar to the E tephra,

and sample 17JF23b was most similar to the C or Z2 tephras (Table 3B). The geochemistry data were combined with a comparison of the field appearance, pumice mineralogy, and mapped isopachs of the major tephras outlined in the literature.

Geochronology

The $^{40}Ar/^{39}Ar$ geochronology method was applied to a granite sampled within the Amatitlan caldera and a granite sampled at location 4. Results from $^{40}Ar/^{39}Ar$ dating of the two samples are displayed in Table 4 (full data table in Supplemental Material[1]). Feldspar grains were picked from crushed bulk samples of both granite samples. Feldspar (500–1000 μm) was isolated from both of the samples via crushing, sieving, and magnetic sorting. The feldspar was treated with 10% HF in an ultrasonic bath for 5 min and then rinsed thoroughly with deionized water. The leached feldspar separates were wrapped in an aluminum foil packet and irradiated with 28.201 Ma Fish Canyon tuff sanidine (FCs). At the University of Wisconsin–Madison WiscAr Laboratory, single feldspar crystals were incrementally heated using a 25 W CO_2 laser and analyzed using a MAP 215–50 mass spectrometer following the procedures outlined in Jicha and Kay (2018). The age uncertainties shown in Table 4 and Figure 11 reflect analytical contributions at the 2σ level; the decay constants are from Min et al. (2000). Mass discrimination was assessed by analysis of atmospheric argon prior to and following the analytical session, and it was calculated using a linear law relationship relative to $^{40}Ar/^{39}Ar = 298.56 \pm 0.31$ (Lee et al., 2006). Ages were calculated relative to a FCs standard age of 28.201 Ma (Kuiper et al., 2008).

New GPS Site Velocities and Elastic Block Model

We processed all the new GPS data with methods described by Ellis et al. (2018). We then updated the elastic block model of Ellis et al. (2019) in two stages. We first assimilated all the new GPS position time series into the time-dependent regional

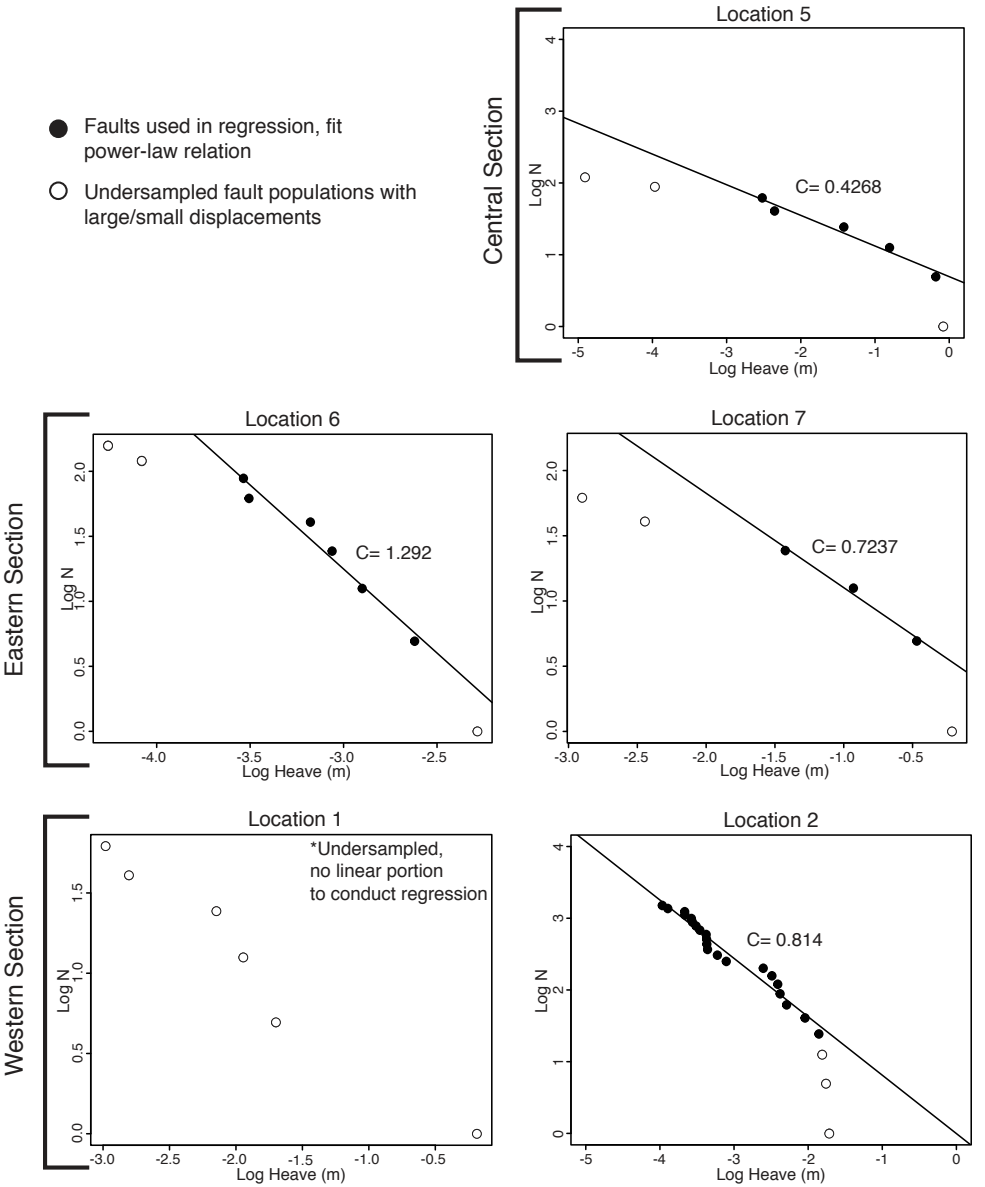

Figure 9. Frequency-displacement plots for locations 1, 2, 5, 6, and 7. Regression lines were fitted to the linear portion of the data to determine the slope (*C*; black points). The value of *C* was used to determine the amount of elongation due to the undersampled population of small faults. All fault samples, except location 1, had linear portions on which to conduct a regression.

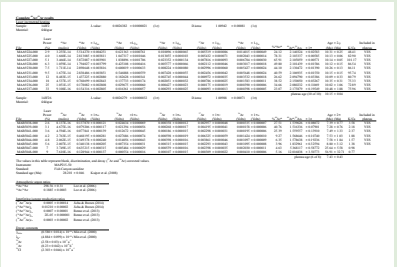

[1]Supplemental Material. Complete $^{40}Ar/^{39}Ar$ results. Please visit https://doi.org/10.1130/GEOS.S.13166516 to access the supplemental material, and contact editing@geosociety.org with any questions.

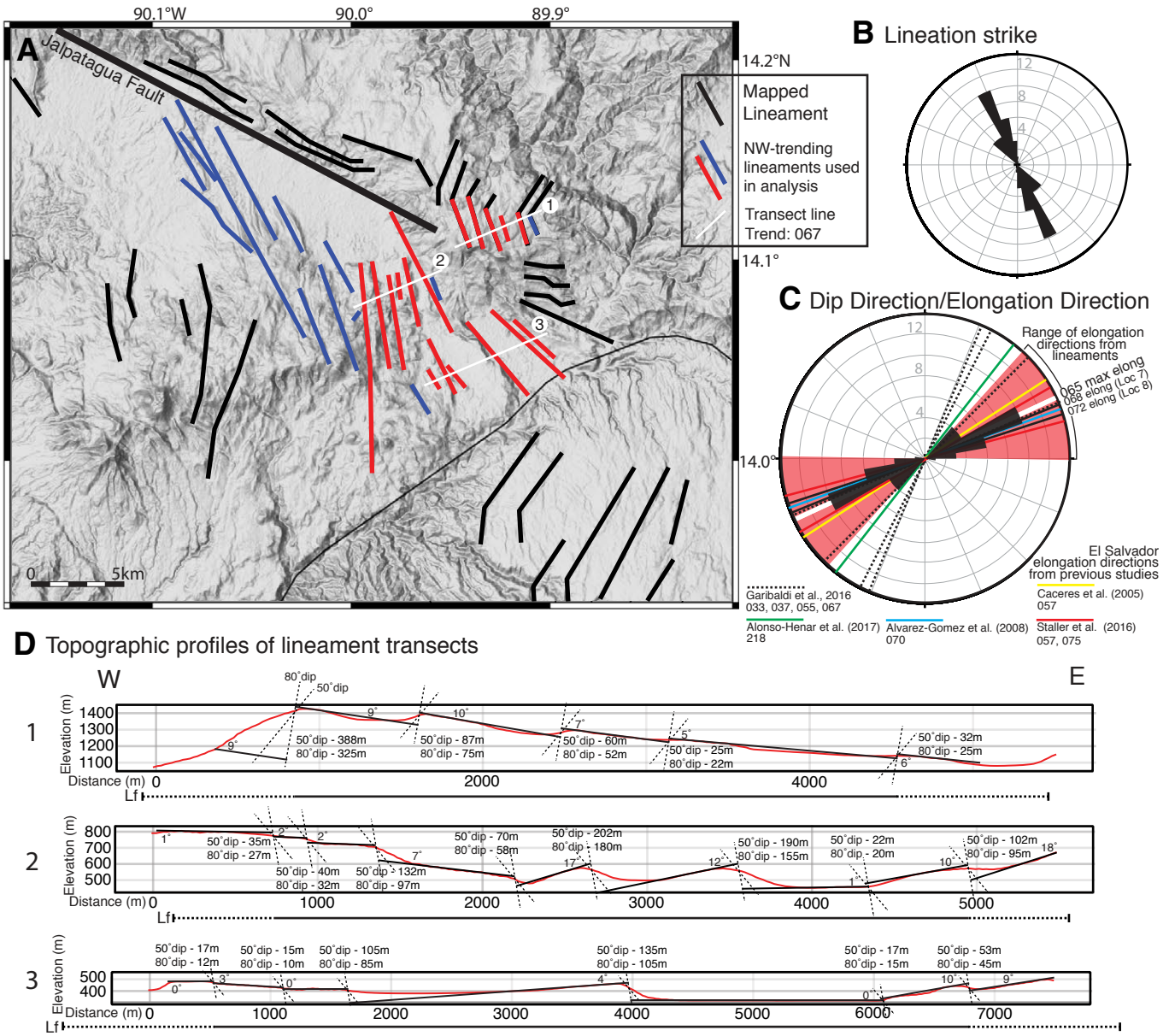

Figure 10. (A) Mapped lineaments near the eastern termination of the Jalpatagua fault. Blue and red lineaments were all used for estimating the general maximum elongation direction. Red lineaments signify those used in the transects (white lines). (B) Rose diagram of lineament strike. (C) Rose diagram of the assumed dip direction of lineaments and other elongation data from this work and previous work in the El Salvador fault system. (D) Topographic profiles of the three lineament transects (white lines from A) with interpretations of offset horizons and offset amounts. Lf—final length of transect.

TABLE 3A. X-RAY FLUORESCENCE (XRF) RESULTS

Sample ID:	17JF23a	17JF23b	17JF26	17JF65	14JF2	WH19S1	WH19S2
Location:	1	1	Within Amatitlan caldera	3	4	7 (lower)	7 (upper)
Latitude (°N):	14.49°	14.49°	14.45°	14.25°	14.25°	14.05°	14.05°
Longitude (°W):	90.60°	90.60°	90.52°	90.22°	90.20°	89.90°	89.90°
Normalized major elements (wt%)							
SiO_2	71.42	68.87	75.14	79.58	78.16	66.56	66.67
TiO_2	0.403	0.354	0.219	0.120	0.131	0.706	0.707
Al_2O_3	14.88	16.26	13.67	11.56	12.21	15.98	16.03
FeO*	2.45	3.27	1.50	0.97	0.73	4.51	4.64
MnO	0.098	0.144	0.048	0.060	0.068	0.179	0.179
MgO	0.67	1.03	0.22	0.13	0.16	1.08	1.03
CaO	2.02	3.55	1.06	1.32	0.50	2.82	2.92
Na_2O	4.16	4.24	3.89	2.02	3.69	5.25	4.86
K_2O	3.81	2.10	4.22	4.23	4.35	2.70	2.75
P_2O_5	0.091	0.181	0.039	0.003	0.019	0.220	0.209
Total	100.00	100.00	100.00	100.00	100.00	100.00	100.00
Unnormalized trace elements (ppm)							
Ni	4	5	6	5	2	2	2
Cr	4	2	5	4	5	3	2
Sc	4	5	3	2	1	16	17
V	29	24	18	10	5	25	28
Ba	1007	801	560	1433	749	1019	995
Rb	100	45	166	84	138	63	64
Sr	211	441	125	171	60	262	268
Zr	247	142	146	93	87	197	196
Y	23	18	25	19	16	41	40
Nb	6.6	4.2	9.8	9.1	7.0	3.8	4.0
Ga	15	15	17	13	13	17	18
Cu	6	3	13	2	1	6	10
Zn	50	62	30	27	18	89	87
Pb	15	9	14	14	17	10	9
La	18	14	28	21	17	17	18
Ce	47	33	58	44	29	39	35
Th	8	3	13	8	12	4	4
Nd	21	16	21	18	11	23	23
U	3	1	4	3	1	2	3

TABLE 3B. SIMILARITY COEFFICIENTS BETWEEN GEOCHEMISTRY OF COLLECTED SAMPLES AND MAJOR QUATERNARY TEPHRAS

Tephra	17JF23a	17JF23b
I falls	0.85	0.74
E	0.92	0.67
C	0.76	0.86*
H flow, low K average	0.79	0.68
H flow, high K average	0.60	0.47
H fall average	0.63	0.50
Tflow	0.86	0.62
Tt fall	0.86	0.62
Z5	0.88	0.66
Z4	0.89	0.67
Z2	0.70	0.87
W flow average	0.74	0.61
W fall average	0.76	0.67
Lf(2)	0.89	0.64
Lf(1)	0.82	0.65
Lt	0.84	0.62

*Best correlation for sample 17JF23a between the two highest similarity coefficients. Shading indicates the pairs with the greatest similarity coefficients.

TABLE 4. RESULTS OF $^{40}Ar/^{39}Ar$ ANALYSIS

Sample no.	Location	SiO_2 (wt%)	Latitude (°N)	Longitude (°W)	Material	$^{40}Ar/^{36}Ar_i \pm 2\sigma$	Isochron age (Ma ± 2σ)	*N*	^{39}Ar (%)	MSWD	Plateau age (Ma ± 2σ)
17JF26	Amatitlan Caldera	75.1	14.4516	90.5151	Feldspar	300.0 ± 3.3	7.25 ± 0.59	6 of 8	94.7	0.20	7.43 ± 0.43
17JF2	Location 4	78.2	14.2472	90.2018	Feldspar	300.1 ± 1.8	10.11 ± 0.05	10 of 10	100.0	0.80	10.15 ± 0.04

Note: Ages were calculated relative to 28.201 Ma Fish Canyon sanidine standard (Kuiper et al., 2008) using the decay constants of Min et al. (2000). Atmospheric $^{40}Ar/^{36}Ar$ = 298.56 ± 0.31 (Lee et al., 2006). MSWD—mean square of weighted deviates.

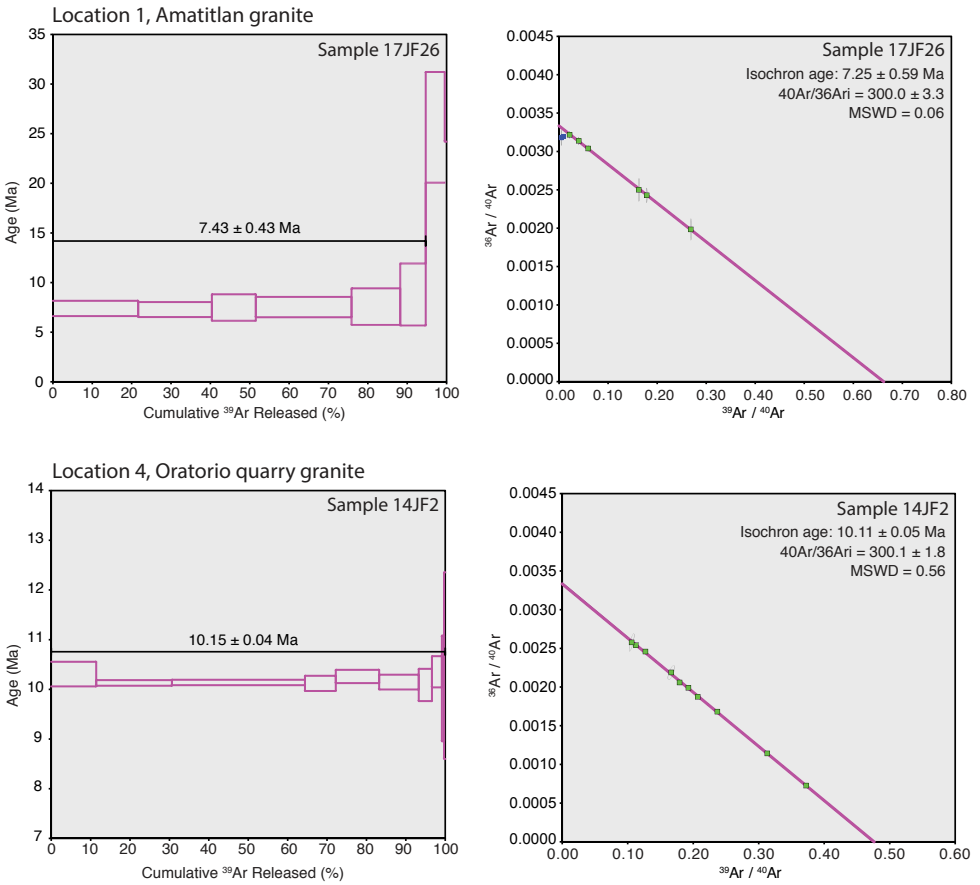

Figure 11. $^{40}Ar/^{39}Ar$ age plateau and isochron plots for feldspars from location 1, Amatitlan granite (sample 17JF26), and location 4, Oratorio quarry granite (sample 14JF2). Age spectra for each sample are on the left, with inverse isochron plots on the right. MSWD—mean square of weighted deviates.

elastic model described by Ellis et al. (2018) in order to correct the new and existing regional GPS time series for the effects of large earthquakes in 2009 and 2012. Figure 5 displays the updated velocities for GPS sites in our study area relative to a stationary Caribbean plate. Following methods described in Ellis et al. (2019), we then inverted the new 200+ station regional GPS velocity field from the updated time-dependent model to estimate a revised elastic block model (Fig. 5B).

Principal Strain Axes from GPS Velocities

With increased GPS coverage near the eastern termination and near locations of measured faults and lineaments, principal strain rate axes were estimated from GPS site velocities to compare to the strain estimated from fault data (Fig. 12). To facilitate the comparison between infinitesimal strain that was estimated from GPS site velocities and finite strain estimated from our fault/lineament analyses, we first corrected the GPS site velocities for the effects of elastic deformation from locked faults in the block model (which is one output of the elastic block model). Using the application SSPX, which calculates a best-fitting strain rate tensor (2-D) from three or more GPS site velocities (Cardozo and Allmendinger, 2009, 2019), we inverted the velocities for GPS sites ZAPO, DANT, and MOYU, which surround the faults we measured at locations 6 and 7 (Fig. 12B).

RESULTS

Paleostress

The mean σ3 orientation for fault slip data from locations 3, 4, and 5 was 266/04, with mean σ1 orientations of 175/09 for strike-slip faults (black dots; Fig. 6) and 261/82 for normal faults (white dots; Fig. 6). All locations suggested approximately E-W tension for faulting observed along the Jalpatagua fault, whether resulting in strike-slip or normal faulting. The σ3 orientations for locations 6 and 7 (eastern section) showed a wider variance and 95% cone of confidence than those from the central section. The main cluster for the eastern section, identified by contouring, indicated σ3 orientations with a mean of 066/09. The σ1 orientations showed a mean of 259/83.

Maximum Elongation

With the elongation analysis, we observed that normal faults suggest 0.6% and 43.5% of ENE- and ESE-oriented elongation, respectively, in the Amatitlan caldera (western section), 17.8% of nearly E-W elongation along the Jalpatagua fault (central section), and 7.2% and 33% of NE-oriented elongation at the Guatemala–El Salvador border (eastern section; Fig. 8; Table 2). Revised elongation increased 250%, 115%, and 200% due to elongations from small, unsampled faults (locations 2, 5, and 7, respectively). The inclusion of small, unsampled faults accounted for 52%, 11%, and 45% of the revised elongations at locations 2, 5, and 7, respectively.

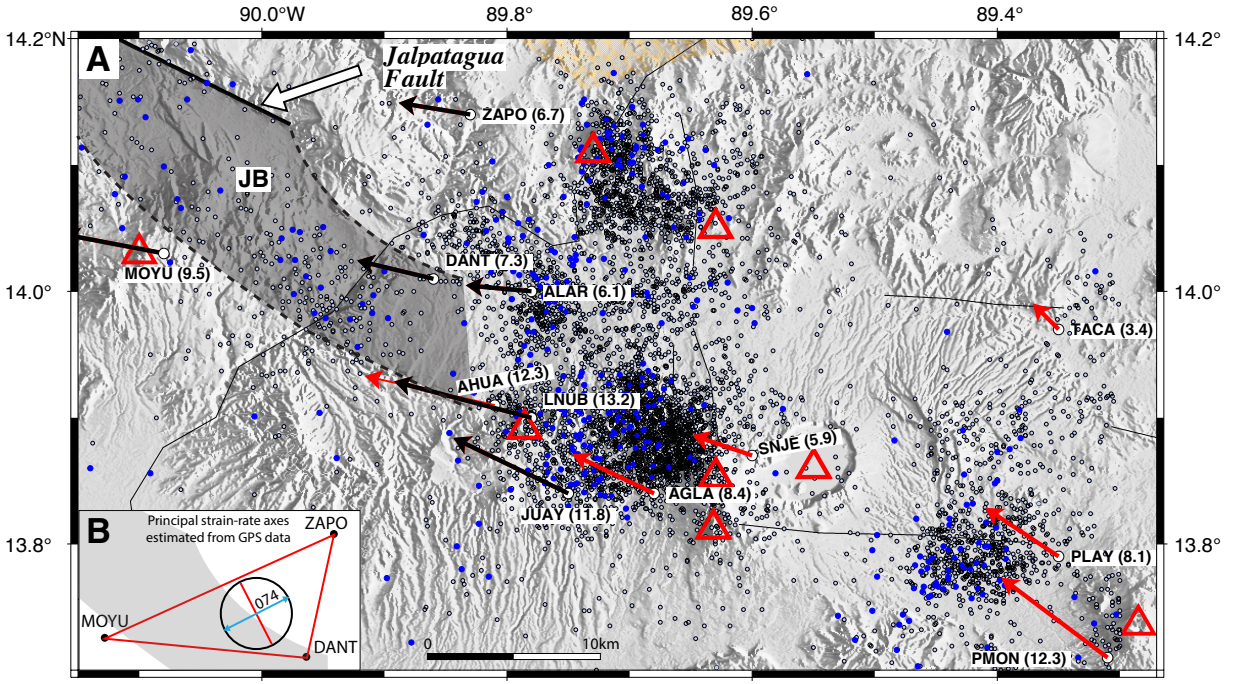

Figure 12. (A) Global positioning system (GPS) site velocities relative to the Caribbean plate and microearthquakes near eastern termination of the Jalpatagua fault and in western El Salvador. Sites with red arrows have velocities derived using the same GPS data as in Ellis et al. (2018, 2019). Sites with black arrows have velocities that incorporate all the data from Ellis et al. (2018, 2019) and additional observations described in the text. Velocities for sites ALAR, DANT, and JUAY have not been reported previously and were incorporated in the new GPS velocity field inversion described in the text. Red triangles indicate volcanic centers. The microearthquakes, which are from the Ministry of the Environment (*MARN*) earthquake catalog (http://www.marn.gob.sv/category/avisos/sismologia/), span 1984 to mid-2019 and are limited to depths shallower than 20 km. Blue and black/light blue circles are for microseisms with local magnitudes greater than 3.0 and magnitudes 1–3, respectively. Gray area with black dashed border outlines the Jalpatagua pull-apart basin (JB), based on geomorphic lineaments and supported by the area of microearthquakes within the basin and differential velocities between GPS sites ZAPO-MOYU and DANT-AHUA/LNUB. (B) Schematic map of GPS sites used to estimate principal strain rate axes. Red triangle connects the GPS sites used to estimate a maximum elongation orientation of 074° (infinitesimal strain) for the area that includes the Jalpatagua pull-apart basin (gray area).

Lineaments

If we assume lineaments represent normal faults with trend-perpendicular fault movement, the collected data would indicate an elongation direction of ~065°. Estimated elongations for the three transects ranged from 0.5% to 10.3% (Table 5). While we also used topography as a marker surface and assumed 50°–80° fault dips to estimate elongation across lineament transects, this method provides a conservative estimate of elongation (Fig. 10).

Geochemistry

Based on similarity coefficients and field evidence, sample 17JF23a from location 1 best correlates to the E tephra, a 51 ka tephra from the Amatitlan complex, and sample 17JF23b best correlates to the C tephra, a 54 ka tephra from a source near the Amatitlan caldera (Table 1; Fig. 2; Koch, 1970; McLean, 1970; Koch and McLean, 1975; Wunderman and Rose, 1984; Rose et al., 1987, 1999; Schindlbeck et al., 2016). In the eastern section, the two tephra deposits collected from location 7 (samples WH19S1 and WH19S2; Table 1) do not correlate to any of the major Quaternary ashes, based on location and thickness of depositions. The light color, large thickness, and presence of mafic lithics and pumice suggest a possible origin from

the Moyuta volcano to the southwest of the outcrop, which is suggested to have output andesite and eruptive material during the Quaternary (Bethancourt et al., 1976).

Geochronology

A $^{40}Ar/^{39}Ar$ age of 7.43 ± 0.43 Ma was determined for the Amatitlan granite, and an age of 10.15 ± 0.04 Ma was determined for the location 4 granite (Fig. 11). We attempted to determine the age of the unfaulted pyroclastic flow from location 2 (sample 17JF13) using the $^{40}Ar/^{39}Ar$ dating technique on phenocrysts, but it contained no radiogenic argon. This approach indicates that the pyroclastic flow is likely younger than 50 ka.

GPS Site Velocities and Elastic Block Model

In the vicinity of the Jalpatagua fault, our newly derived elastic block model (Fig. 5B) predicted that the forearc sliver moves 7.1 ± 1.8 mm yr^{-1} toward N65°W ± 14° relative to the lithosphere north of the Jalpatagua fault (defined as the Ipala block by Ellis et al., 2019). The updated velocity is ~10% slower than and more parallel to the 295°-striking Jalpatagua fault trace than that predicted by the Ellis et al. (2019) block model (inset in Fig. 5B), although the velocities predicted by both models agree within their respective 1σ uncertainties.

Relevant to the terminations of the Jalpatagua fault, which are difficult to define based on its morphology, our new elastic block model indicated that slip between the forearc sliver and backarc west of the Guatemala City graben averages 2–3 mm yr^{-1}, in accord with results reported by Ellis et al. (2019), but not significantly different than zero within the 95% slip rate uncertainties. At the eastern termination of the Jalpatagua fault, the absence of a velocity gradient between GPS sites ZAPO, DANT, and ALAR in western El Salvador, which are located directly east of the eastern mapped extent of the fault (Fig. 12), clearly indicates that the fault does not continue linearly along its trajectory into western El Salvador. Instead, a 5–6 mm yr^{-1} velocity increase occurs between GPS sites ALAR, DANT, and ZAPO north of the volcanic arc and GPS sites AHUA, LNUB, and JUAY within or south of the volcanic arc (Fig. 12). Therefore, dextral slip across the Jalpatagua fault and any other active structures adjacent to the fault steps 20–25 km southward in westernmost El Salvador.

TABLE 5. ELONGATION CALCULATIONS FOR LINEAMENT TRANSECTS

Transect	No. of faults	Final length, Lf (m)	Avg. spacing (m)	Lf + 2FS (m)	dL (80°–50°) (m)	E (80°–50°) (%)
1	5	3680	927.5	5535	87–381	1.6–7.4
2	8	4230	610.0	5450	115–510	2.2–10.3
3	6	7260	1248.0	9756	47–220	0.5–2.3

Notes: Lf—final length of transect; FS—fault spaces (based on average spacing); dL—change in transect length due to fault movement; E—elongation.

Principal Strain Axes from GPS Velocities

The best-fitting strain rate ellipse has a maximum extension of 1.03 × 10^{-7} yr^{-1} toward 074° and a minimum extension of –0.7 × 10^{-7} yr^{-1} toward 344° (Fig. 12B). These directions are consistent with the principal paleostress orientations estimated from locations 6 and 7.

DISCUSSION

Deformation Model of Southeastern Guatemala

Results from the analyses above indicate that faulting differs in each of the three studied areas along the Jalpatagua fault. Results from each area will be discussed individually followed by our proposed model of deformation.

Central Section

Paleostress analysis of strike-slip and normal faults along the Jalpatagua fault (locations 3, 4, and 5) indicates an E-W–directed σ3 (266°) with shallow approximately NNW-N–oriented σ1 from strike-slip faults (nearly vertical σ2) and nearly vertical σ1 from normal faults (shallow N-oriented σ2; Fig. 6). These paleostress orientations are consistent with a stress regime that could produce dextral slip along a fault in the orientation of the Jalpatagua fault along with N-striking normal faults. A NNW-N–oriented σ1 also agrees with the Riedel shear model, as it should bisect the small angle between R and R′ shears (sets 1 and 2 from strike-slip fault subsets; Fig. 2; Tchalenko, 1970; Logan et al., 1979). Strain analysis of minor normal faults indicates that 17.8% elongation has occurred at one outcrop along the Jalpatagua fault in an E-W orientation (Fig. 8). E-W elongation along the Jalpatagua fault parallels the E-W elongation recorded geodetically across N-S–oriented grabens to the north of the Jalpatagua fault (Rodriguez et al., 2009; Ellis et al., 2019). In general, N-S–oriented normal faults and the four subsets of strike-slip fault orientations (including one orientation parallel to the Jalpatagua fault and velocity orientation of the forearc sliver) support dextral Jalpatagua movement, define the orientations of Jalpatagua-typical minor faulting, and are consistent with our revised GPS data and model (Fig. 13).

Various faulted lithologies were observed along the Jalpatagua fault, from 10.15 ± 0.04 Ma (Miocene) granite and Miocene welded tuff to nonindurated Quaternary tephras. The Miocene age for the quarry granite sample at location 4, as well as the Amatitlan caldera granite sample, agrees with other intrusive rocks dated from the Atitlan caldera (8.5–13.8 Ma; $^{40}K/^{40}Ar$ ages) and the Santa Rosa caldera (15.7 ± 0.06 Ma; $^{40}K/^{40}Ar$ age) along the arc (Williams and McBirney, 1969; Reynolds, 1987; Patino, 2007).

The absence of unfaulted units suggests that Jalpatagua-related deformation has continued since the deposition of the most recent observed

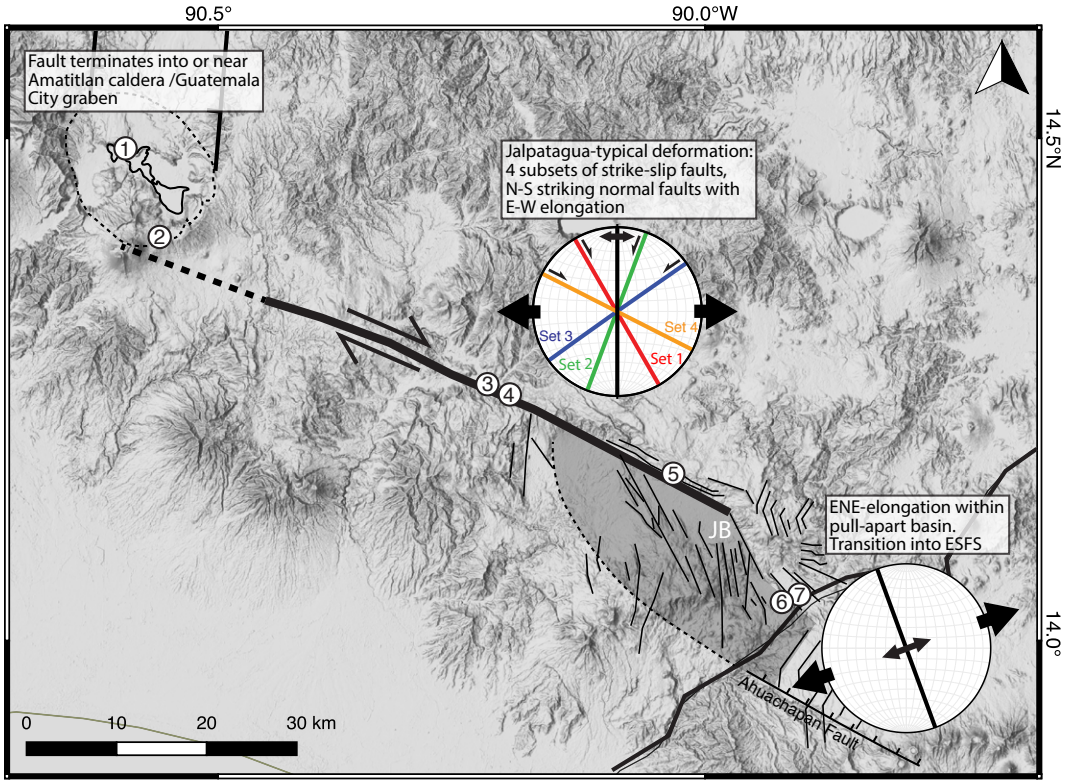

Figure 13. Preferred model for faulting along the Jalpatagua fault. Each stereonet indicates the average orientation of fault arrays (and respective motions) collected in the central and eastern sections. Large black arrows also indicate the elongation orientations for each section. Near the eastern termination, dashed lines and shading outline the Jalpatagua pull-apart basin (JB). Near the western termination, the dashed black line connects the Jalpatagua fault termination and the southern extension of the Guatemala City graben. ESFS—El Salvador fault system.

Quaternary deposit. The absence of unfaulted units and a current slip rate of ~7.1 mm yr^{-1} across the Jalpatagua fault suggest that dextral movement and associated normal faulting are still active along the Jalpatagua fault trace. None of our observations defined a minimum age or total offset for the Jalpatagua fault.

Eastern Section

Our paleostress analysis of minor normal faults near the Guatemala–El Salvador border, and eastern termination of the Jalpatagua fault, indicates ENE-oriented σ3 (066°) and vertical σ1 orientations, which support extensional deformation in this area with ENE-directed elongation. A comparison of the E-W–oriented and ENE-oriented σ3 orientations of the central and eastern sections, respectively, indicates that the two σ3 orientation samples are significantly different. The 95% confidence cones from each section do not overlap, nor do the related trend boundaries from each cone (Fig. 6). This lack of overlap indicates that it is unlikely that central and eastern section fault data belong to the same fault population (faults creating similar σ3 orientations). This significant difference suggests that our faulting evaluation should treat the data from the two areas as separate and that the change of the σ3 orientations may reflect a real change in faulting behavior near the eastern termination of the Jalpatagua fault.

The results from our strain analysis estimated that normal faults accommodate 7.2% and up to 33% of ENE-oriented elongation (068° and 072°), with NW-trending fault traces (lineaments) in the same area suggesting 0.5%–10% of similarly oriented elongation (065°; Fig. 8). While ENE-oriented elongation in the eastern section differs from observations along the central section of the Jalpatagua fault, NE-oriented elongation is consistent with orientations calculated from normal faults measured within the adjacent, western El Salvador fault system (Cáceres et al., 2005; Canora et al., 2014; Garibaldi et al., 2016). The observed fault traces also extend from the eastern end of the Jalpatagua fault, toward the Ahuachapan fault to the SE in El Salvador, a southern bounding fault of the El Salvador fault system (Figs. 10 and 13).

Microearthquakes also provide useful evidence about the eastern termination of the Jalpatagua

fault (circles in Fig. 12). Excluding microearthquakes within a few kilometers of GPS sites LNUB and SNJE, where seismically active volcanic sources are located, numerous microearthquakes are distributed within a N-S–trending band to the east and southeast of the Jalpatagua fault. The GPS sites to the east and west of and within this seismically active region define an ~6 mm yr^{-1} E-to-W velocity gradient that is indicative of active approximately E-W–dominated stretching (Fig. 12A). Together, the microearthquakes and pattern of the GPS site velocities indicate that dextral slip at the eastern terminus of the Jalpatagua fault near the El Salvador–Guatemala border is transferred southward by structures within an extensional step-over in the volcanic arc.

In the absence of age markers, we could not calculate strain rates for minor faulting near the eastern termination. However, we could make a comparison between maximum elongation directions and the principal strain rate axes estimated from GPS velocity data. The principal strain rate axes estimated from GPS stations ZAPO, DANT, and MOYU, which surround locations 6 and 7, indicate a maximum extension orientation of 074° (Fig. 12B), indistinguishable from the maximum elongation directions of 068°, 073°, and 067° for normal faults and lineaments (Fig. 10). Similar to observations along the Jalpatagua fault, all observed Neogene and Quaternary deposits within the eastern section were faulted without an overlying, unfaulted layer. The elongation orientations for the GPS and faulting data, which span much different time scales (present and Quaternary/Neogene), are thus consistent. Therefore, faulting occurred after the most recent deposit in this area and is likely still active, as ENE elongation is recorded by the GPS data as well.

With the GPS velocity orientations, microearthquakes, and observed NW-oriented faults, we defined and outlined a pull-apart basin in this zone (labeled Jalpatagua basin) that accommodates transtension and transition between the eastern termination of the Jalpatagua fault and the western El Salvador fault system (shaded and outlined as JB in Figs. 12 and 13). Other mechanisms, such as vertical axis rotation, could also create ENE elongations in a right step-over of this dextral fault system. However, the similarity in principal axes of infinitesimal strain and overall strain suggest coaxial deformation rather than rotation.

Western Section

The only observations of faulting past the western termination of the Jalpatagua fault, near El Cerinal, were located within the Amatitlan caldera, at two outcrops dominated by normal faults (Fig. 2). Faults were exposed because of new highway construction, and many were subsequently covered with concrete.

Estimated elongation directions and amounts differed from 0.6% approximately ENE-directed elongation on the north side of the caldera, to up to 43.5% ESE-directed elongation on the southern side of the caldera (Fig. 8). The lithologies and timing of faulting also differed. Faulting at location 1 (north side) suggests that faulting occurred before deposition of tephra E (51 ka; Schindlbeck et al., 2016), after deposition of tephras E and C (54 ka), and before deposition of the most recent Amatitlan J tephras, which are unfaulted at location 1 (Fig. 3; Koch and McLean, 1975). Faulting at location 2 (south side) indicates that faulting occurred before deposition of a white, pyroclastic flow, most likely younger than 50 ka. We did not observe evidence of active faulting within the caldera.

Two observations suggest that the faulting within the Amatitlan caldera is more likely a result of past caldera-related events, rather than Jalpatagua-related movement. First, elongation orientations are roughly parallel to the caldera rim at each location, rather than parallel to E-W elongations observed along the Jalpatagua fault. Second, we did not find field evidence—of either a through-going fault or a minor fault array—that supports the presence of an active fault transecting the Amatitlan caldera. Furthermore, there is no evidence of a through-going fault in the area between the caldera and the western terminus of the Jalpatagua fault trace.

GPS data also indicate that little to no deformation occurs along the volcanic arc west of the Guatemala City graben (Fig. 5; Ellis et al., 2019). We concluded that the Jalpatagua fault thus terminates near the Amatitlan caldera (Fig. 13). Our evidence does not rule out a past connection between the Amatitlan caldera and the Jalpatagua fault, which has been proposed by Eggers (1971), Wunderman (1982), and Wunderman and Rose (1984) based on the linearity of the Amatitlan lake. Additionally, N-S–striking normal faults have been mapped within the caldera (Eggers, 1971), and they are parallel to N-S–striking normal faults measured at location 5 along the Jalpatagua fault to the east. Last, recent earthquake swarms occurred on the west and east sides of the caldera, respectively, in 2019 and 2020.

Role of the Jalpatagua Fault in the Central American Forearc System

Our analysis of minor faulting and updated GPS velocities in southeastern Guatemala indicates that: (1) the faulting is related to dextral movement along the Jalpatagua fault; and (2) the fault arrays accommodate E-W elongation. Our evidence more clearly defines how and where the Jalpatagua fault terminates at each end (Fig. 13). At its eastern end, secondary faults record ENE-oriented elongation in a pull-apart basin, parallel to elongation estimated within the El Salvador fault system to the east. The presence of the pull-apart basin is further supported by the GPS data, which record transtension in the area of a right step-over. At its western end, faulting is only observed within the Amatitlan caldera, but it appears more related to caldera-forming events rather than Jalpatagua fault movement. We were unable to locate any major fault/lineament west of the Guatemala City graben that could accommodate dextral motion of the forearc. Ellis et al. (2019) reached similar conclusions regarding the absence of a through-going dextral fault within the volcanic arc based on their GPS measurements from sites west of the Guatemala City graben.

The Guatemala City graben may be related to the termination of the Jalpatagua fault. The termination of any strike-slip fault would typically result in an area of local extension, often characterized by an extensional horsetail structure. In the case of the dextral Jalpatagua fault, this extensional area

would be located *north* of its western termination. In fact, both the Amatitlan caldera and the southward termination of the Guatemala City graben occur in this area of inferred extensional deformation. Additionally, the N-S–striking faults mapped within the caldera parallel the N-S–striking Guatemala City graben (and other grabens in eastern Guatemala) and normal faulting observed along the Jalpatagua fault, and they could be associated with similar E-W elongation as recorded in both areas. Alternatively stated, the Jalpatagua fault terminates on its western end into diffuse extensional structures possibly connected to the active volcanic arc, Amatitlan caldera, and/or N-S–striking bounding faults of the Guatemala City graben (dashed line in Fig. 13).

Similarly, distributed extension also occurs on the *southern* side of the eastern termination of the Jalpatagua fault, where dextral slip on the Jalpatagua fault is transferred southeastward across a pull-apart basin (light shaded area in Fig. 13) to the western terminus of the El Salvador fault system. The Jalpatagua basin, located south of the fault, appears to initiate near the midpoint of the Jalpatagua fault and curve to the south and east, nearly connecting to the southern bounding Ahuachapán fault of the El Salvador fault system (Fig. 13). Within this lenticular-shaped basin, the observed NW-trending faults and lineaments also extend toward and connect to the terminations of the two main faults, recording ENE elongation. Normal fault focal mechanisms indicating E-W extension have also been recorded south of the Jalpatagua fault, near the western edge of the pull-apart basin (Ellis et al., 2019). With the WNW-trending Jalpatagua fault connecting to the E-W–trending strike-slip faults of the El Salvador fault system, it makes sense that the pull-apart basin shows evidence of complex internal geometry and transtensional deformation to accommodate the transition between two nonparallel faults.

Finally, two differences between the Jalpatagua fault and the El Salvador fault system should be addressed to aid in understanding along-strike variations in forearc systems: (1) the difference in orientation (WNW-oriented Jalpatagua fault and approximately E-W–oriented El Salvador fault system); and (2) the difference in complexity (continuous fault vs. en échelon fault system; Fig. 1). Both differences may be attributed to the absence/presence of an active volcanic arc. It may be more favorable for the Jalpatagua fault to maintain a stable, singular structure due to the lack of active volcanic sources along the fault trace. The orientation of the Jalpatagua fault satisfies a simple model of strain partitioning, with linear dextral movement occurring parallel to the trench, through a variety of volcanic lithologies, but no active sources. In contrast, deformation along the El Salvador fault system may be more diffuse due to the presence of multiple large volcanic centers. The E-W orientation of the diffuse fault system still accommodates trench-parallel motion, with movement along multiple right-stepping strike-slip faults.

Overall, slip along the Central America forearc boundary decreases westward and terminates near or into the Guatemala City graben. With 12.5 mm yr^{-1} of dextral slip occurring in Nicaragua across a wide zone of bookshelf faults, and 10.3 mm yr^{-1} to 9.7 mm yr^{-1} (west to east) occurring across the El Salvador fault system, forearc motion decreases further to 7.1 mm yr^{-1} across the Jalpatagua fault, and no movement (or very minor) or through-going fault is recorded across the Amatitlan caldera and volcanic arc to the west (Ellis et al., 2019). The slip rate decreases toward the Guatemala City graben, which is the westernmost structure accommodating E-W elongation to the north of the forearc boundary (Ellis et al., 2019). A similar westward decrease in slip rate toward the Guatemala City graben is observed across the sinistral Motagua fault, on the northern extension of the Guatemala City graben (Ellis et al., 2019). Overall, the secondary faulting presented in this study characterizes the deformation related to dextral movement on the Jalpatagua fault, and the extensional deformation that occurs across a fault transition (eastern termination) and near the end of a large dextral boundary (western termination).

CONCLUSIONS

Our analysis of GPS site velocities and secondary faulting in southeastern Guatemala and westernmost El Salvador more clearly defines deformation along the Jalpatagua fault system, as follows:

Along the central section of the Jalpatagua fault:

(1) Elastic block modeling of new and updated GPS site velocities gives a revised dextral slip rate of 7.1 ± 1.8 mm yr^{-1} for the Jalpatagua main fault and adjacent forearc structures.

(2) Jalpatagua-related minor faulting is characterized by four sets of strike-slip faulting (330°, 020°, 055°, and Jalpatagua-parallel 295°) and N-S normal faulting. Minor fault orientations support deformation related to dextral movement. At one outcrop, minor normal faulting accommodated 17% of E-W elongation, paralleling E-W elongation observed across grabens to the north.

(3) A $^{40}Ar/^{39}Ar$ age of 10.15 ± 0.04 Ma was determined for a granite (location 4) collected along the Jalpatagua fault, supporting active faulting.

At the eastern termination of the Jalpatagua fault:

(1) GPS and microearthquake data indicate that the Jalpatagua fault does not continue linearly into El Salvador. Dextral offset can be observed between GPS sites southeast of the termination, indicating a complex right step-over into western El Salvador. The location of microearthquakes shows that complex strike-slip and extensional structures accommodate the transition between the Jalpatagua fault and the El Salvador fault system. Principal strain rate axes calculated from GPS velocities indicate a NE-oriented maximum extension (074°) within the transition area.

(2) NW-striking normal faults and lineaments near the eastern termination record NE-trending elongations (elongation estimates between 7% and 33%). The NE-directed elongation directions are statistically different than E-W elongations observed along the Jalpatagua fault, and parallel to minor faulting observed within the El Salvador fault system.

(3) GPS data, minor fault and lineament data, and geomorphology outline a transtensional pull-apart basin connecting the Jalpatagua fault to the El Salvador fault system.

At the western termination of the Jalpatagua fault, in the vicinity of the Amatitlan caldera and the southern extension of the Guatemala City graben:

(1) GPS site velocities indicate that discrete dextral movement of the Jalpatagua fault terminates east of, or near, the Guatemala City graben/Amatitlan caldera. West of the Guatemala City graben, little to no movement occurs across the volcanic arc.

(2) Normal faulting observed within the Amatitlan caldera is more likely related to caldera-forming events than Jalpatagua fault movement, with elongation directions parallel to the caldera rim and stratigraphic evidence indicating past faulting events.

(3) A $^{40}Ar/^{39}Ar$ age of 7.43 ± 0.43 Ma was determined for the Amatitlan granite collected within the caldera.

Overall, the Jalpatagua fault is the westernmost structure that accommodates dextral movement of the Central American moving forearc. Dextral offset terminates into extensional structures at each end—a transtensional pull-apart basin to the east and the Guatemala City graben to the west.

ACKNOWLEDGMENTS

This work was funded by the National Science Foundation grant EAR-1144418 (to DeMets). We thank Guatemalan institutions that provided technical and safety support, including the University of Guatemala in Coban, Instituto Nacional de Sismología, Vulcanologia, Meteorologia e Hidrología of Guatemala, and Coordinadora Nacional para la Reducción de Desastres (CONRED) of Guatemala. Special thanks go to David Greene, Joshua Rodenas, Roberto Mérida Boogher, and Carlos Peréz, who aided in field work, as well as to Sergio Mendez Rojas, who aided in laboratory work. Reviews by J. Alonso-Henar, an anonymous reviewer, and Associate Editor C.H. Jones improved the manuscript.

REFERENCES CITED

Alonso-Henar, J., Álvarez-Gómez, J.A., and Martínez-Díaz, J.J., 2014, Constraints for the recent tectonics of the El Salvador fault zone, Central America volcanic arc, from morphotectonic analysis: Tectonophysics, v. 623, p. 1–13, https://doi.org/10.1016/j.tecto.2014.03.012.

Alonso-Henar, J., Schreurs, G., Martínez-Díaz, J.J., Álvarez-Gómez, J.A., and Villamor, P., 2015, Neotectonic development of the El Salvador fault zone and implications for deformation in the Central America volcanic arc: Insights from 4-D analog modeling experiments: Tectonics, v. 34, p. 133–151, https://doi.org/10.1002/2014TC003723.

Alonso-Henar, J., Álvarez-Gómez, J.A., and Martínez-Díaz, J.J., 2017, Neogene–Quaternary evolution from transpressional to transtensional tectonics in northern Central America controlled by Cocos: Caribbean subduction coupling change: Journal of Iberian Geology, v. 43, p. 519–538, https://doi.org/10.1007/s41513-017-0034-2.

Alvarado, D., DeMets, C., Tikoff, B., Hernandez, D., Wawrzyniec, T.F., Pullinger, Mattioli, G., Turner, H.L., Rodriguez, M., and Correa-Mora, F., 2011, Forearc motion and deformation between El Salvador and Nicaragua: GPS, seismic, structural, and paleomagnetic observation: Lithosphere, v. 3, no. 1, p. 3–21, https://doi.org/10.1130/L108.1.

Alvarez-Gomez, J.A., Meijer, P.T., Martinez-Diaz, J.J., and Capote, R., 2008, Constraints from finite element modeling on the active tectonics of northern Central America and the Middle America Trench: Tectonics, v. 27, TC1008, https://doi.org/10.1029/2007TC002162.

Alvarez-Gomez, J.A., Staller Vazquez, A., Martinez-Diaz, J.J., Canora, C., Alonso-Henar, J., Insua-Arevalo, J.M., and Bejar-Pizarro, M., 2019, Push-pull driving of the Central America forearc in the context of the Cocos–Caribbean–North America triple junction: Scientific Reports: Nature Research, v. 9, p. 11164, https://doi.org/10.1038/s41598-019-47617-3.

Angelier, J., 1984, Tectonic analysis of fault slip data sets: Journal of Geophysical Research, v. 89, no. B7, p. 5835–5848, https://doi.org/10.1029/JB089iB07p05835.

Angelier, J., 1994, Fault slip analysis and paleostress reconstruction, *in* Hancock, P.L., ed., Continental Deformation: Oxford, UK, Pergamon Press, p. 53–100.

Angelier, J., Tarantola, A., Valette, B., and Manoussis, S., 1982, Inversion of field data in fault tectonics to obtain the regional stress: I. Single phase fault populations: A new method of computing the stress tensor: Geophysical Journal of the Royal Astronomical Society, v. 69, p. 607–621, https://doi.org/10.1111/j.1365-246X.1982.tb02766.x.

Authemayou, C., Brocard, G., Teyssier, C., Simon-Labric, T., Guittierrez, A., Chiquin, E.N., and Moran, S., 2011, The Caribbean–North America–Cocos triple junction and the dynamics of the Polochic-Motagua fault systems: Pull-up and zipper models: Tectonics, v. 30, TC3010, https://doi.org/10.1029/2010TC002814.

Authemayou, C., Brocard, G., Teyssier, C., Suski, B., Consenza, B., Morán-Ical, S., González-Véliz, C.W., Aguilar-Hengstenberg, M.A., and Holliger, K., 2012, Quaternary seismo-tectonic activity of the Polochic fault, Guatemala: Journal of Geophysical Research, v. 117, B07403, https://doi.org/10.1029/2012JB009444.

Bethancourt, H.R., Dominco, E., Girelli, M., and Pasguaré, G., 1976, La Exploracion del Area Geotermica de Moyuta: Guatemala, Instituto Italo – Latin Americano, INDE, 11 p.

Borchardt, G.A., and Harward, M.E., 1971, Trace element correlation of volcanic ash soils: Soil Science Society of America Proceedings, v. 35, p. 626–631, https://doi.org/10.2136/sssaj1971.03615995003500040040x.

Bott, M.H.P., 1959, The mechanisms of oblique slip faulting: Geological Magazine, v. 96, p. 109–117, https://doi.org/10.1017/S0016756800059987.

Burg, J.-P., Célérier, B., Chaudhry, N.M., Ghazanfar, M., Gnehm, F., and Schnellmann, M., 2005, Fault analysis and paleostress evolution in large strain regions: Methodological and geological discussion of the southeastern Himalayan fold-and-thrust belt in Pakistan: Journal of Asian Earth Sciences, v. 24, p. 445–467, https://doi.org/10.1016/j.jseaes.2003.12.008.

Cáceres, D., Monterroso, D., and Tavakoli, B., 2005, Crustal deformation in northern Central America: Tectonophysics, v. 404, p. 119–131, https://doi.org/10.1016/j.tecto.2005.05.008.

Canora, C., Martínez-Díaz, J.J., Villamor, P., Staller, A., Berryman, K., Álvarez-Gómez, J.A., Capote, R., and Díaz, M., 2014, Structural evolution of the El Salvador fault zone: An evolving fault system within a volcanic arc: Journal of Iberian Geology, v. 40, no. 3, p. 471–488, https://doi.org/10.5209/rev_JIGE.2014.v40.n3.43559.

Cardozo, N., and Allmendinger, R.W., 2009, SSPX: A program to compute strain from displacement/velocity data: Computers & Geosciences, v. 35, p. 1343–1357, https://doi.org/10.1016/j.cageo.2008.05.008.

Cardozo, N., and Allmendinger, R.W., 2019, SSPS: A Program to Compute Strain from Displacement or Velocity Data, Version 6.60: http://www.ux.uis.no/~nestor/work/programs.html (accessed May 2019).

Carey, E., 1976, Analyse Numerique d'un Modele Mecanique Elementaire Applique a l'Etude d'une Population de Failles: Calcul d'un Tenseur Moyen des Contraintes a Partir des Stries de Glissement [Ph.D. dissertation]: Paris, France, University Paris Sud, 138 p.

Carr, M.J., 1974, Tectonics of the Pacific Margin of Northern Central America [Ph.D. thesis]: Hanover, New Hampshire, Dartmouth College, 121 p.

Carr, M.J., 1976, Underthrusting and Quaternary faulting in northern Central America: Geological Society of America Bulletin, v. 87, p. 825–829, https://doi.org/10.1130/0016-7606(1976)87<825:UAQFIN>2.0.CO;2.

Célérier, B., 1988, How much does slip on a reactivated fault plane constrain the stress tensor?: Tectonics, v. 7, no. 6, p. 1257–1278, https://doi.org/10.1029/TC007i006p01257.

Célérier, B., 2018, FSA: Fault & Stress Analysis Software, Version 36.5: http://www.bcelerier.univ-montp2.fr/software/dcmt/fsa/fsa.html (accessed May 2018).

Célérier, B., Etchecopar, A., Bergerat, F., Vergely, P., Arthaud, F., and Laurent, P., 2012, Inferring stress from faulting: From early concepts to inverse methods: Tectonophysics, v. 581, p. 206–219, https://doi.org/10.1016/j.tecto.2012.02.009.

DeMets, C., 2001, A new estimate for present-day Cocos-Caribbean plate motion: Implications for slip along the Central American volcanic arc: Geophysical Research Letters, v. 28, no. 21, p. 4043–4046, https://doi.org/10.1029/2001GL013518.

DeMets, C., Gordon, R.G., and Argus, D.F., 2010, Geologically current plate motions: Geophysical Journal International, v. 181, p. 1–80, https://doi.org/10.1111/j.1365-246X.2009.04491.x.

de Saint Blanquat, M., Tikoff, B., Teyssier, C., and Vigneresse, J.L., 1998, Transpressional kinematics and magmatic arcs, *in* Holdsworth, R.E., Strachan, R.A., and Dewey, F.J., eds., Continental Transpressional Tectonics: Geological Society [London] Special Publication 135, p. 327–340, https://doi.org/10.1144/GSL.SP.1998.135.01.21.

Duffield, W.A., Heiken, G.H., Wohletz, K.H., Maasen, L.W., Dengo, G., McKee, E.H., and Castañeda, O., 1992, Geology and geothermal potential of the Tecuamburro volcano area,

Guatemala: Geothermics, v. 21, no. 4, p. 425–446, https://doi.org/10.1016/0375-6505(92)90001-P.
Eggers, A.A., 1971, The Geology and Petrology of the Amatitlán Quadrangle, Guatemala [Ph.D. dissertation]: Hanover, New Hampshire, Dartmouth College, 221 p.
Ellis, A., DeMets, C., Briole, P., Cosenza, B., Flores, O., Graham, S.E., Guzmán-Speziale, M., Hernández, D., Kostoglodov, V., LaFemina, P., Lord, N., Lasserre, C., Lyon-Caen, H., Maradiaga, M., McCaffrey, R., Molina, E., Rivera, J., Rogers, R., and Staller, A., 2018, GPS constraints on deformation in northern Central America from 1999 to 2017: Part 1. Time-dependent modelling of large regional earthquakes and their post-seismic effects: Geophysical Journal International, v. 214, p. 2177–2194, https://doi.org/10.1093/gji/ggy249.
Ellis, A.P., DeMets, C., Briole, P., Cosenza, B., Flores, O., Guzmán-Speziale, M., Hernández, D., Kostoglodov, V., LaFemina, P., Lord, N., Lasserre, C., Lyon-Caen, H., Rodriguez Maradiaga, M., Molina, E., Rivera, J., Rogers, R., Staller, A., and Tikoff, B., 2019, Deformation in northern Central America from 1999 to 2017 using GPS observations: Part 2. Block rotations, fault slip rates, fault locking, and distributed deformation: Geophysical Journal International, v. 218, p. 729–754, https://doi.org/10.1093/gji/ggz173.
Etchecopar, A., Vasseur, G., and Daignieres, M., 1981, An inverse problem in microtectonics for the determination of stress tensors from fault striation analysis: Journal of Structural Geology, v. 3, no. 1, p. 51–65, https://doi.org/10.1016/0191-8141(81)90056-0.
Fitch, T.J., 1972, Plate convergence, transcurrent faulting, and internal deformation adjacent to Southeast Asia and the western Pacific: Journal of Geophysical Research, v. 77, p. 4432–4460, https://doi.org/10.1029/JB077i023p04432.
Franco, A., Lasserre, C., Lyon-Caen, H., Kostoglodov, V., Molina, E., Gúzman-Speziale, M., Monterosso, D., Robles, V., Figueroa, C., Amaya, W., Barrier, E., Chiquin, L., Moran, S., Flores, O., Romero, J., Santiago, J.A., Manea, M., and Manea, V.C., 2012, Fault kinematics in northern Central America and coupling along the subduction interface of the Cocos plate, from GPS data in Chiapas (Mexico), Guatemala and El Salvador: Geophysical Journal International, v. 189, p. 1223–1236, https://doi.org/10.1111/j.1365-246X.2012.05390.x.
Gapais, D., Cobbold, P.R., Bourgeois, O., Rouby, D., and de Urreiztieta, M., 2000, Tectonic significance of fault-slip data: Journal of Structural Geology, v. 22, p. 881–888, https://doi.org/10.1016/S0191-8141(00)00015-8.
Garibaldi, N., Tikoff, B., and Hernández, W., 2016, Neotectonic deformation within an extensional stepover in El Salvador magmatic arc, Central America: Implication for the interaction of arc magmatism and deformation: Tectonophysics, v. 693, p. 327–339, https://doi.org/10.1016/j.tecto.2016.05.015.
Grocott, J., and Taylor, G.K., 2002, Magmatic arc fault systems, deformation partitioning and emplacement of granitic complexes in the Coastal Cordillera, north Chilean Andes (25°30′S to 27°00′S): Journal of the Geological Society [London], v. 159, p. 425–443, https://doi.org/10.1144/0016-764901-124.
Gross, M.R., and Engelder, T., 1995, Strain accommodated by brittle failure in adjacent units of the Monterey Formation, U.S.A.: Scale effects and evidence for uniform displacement boundary conditions: Journal of Structural Geology, v. 17, no. 9, p. 1303–1318, https://doi.org/10.1016/0191-8141(95)00011-2.
Guzmán-Speziale, M., 2001, Active seismic deformation in the graben of northern Central America and its relationship to the relative motion of the North America–Caribbean plate boundary: Tectonophysics, v. 337, p. 39–51, https://doi.org/10.1016/S0040-1951(01)00110-X.
Guzmán-Speziale, M., Valdes-Gonzalez, C., Molina, E., and Martin Gomez, J., 2005, Seismic activity along the Central America volcanic arc: Is it related to subduction of the Cocos plate?: Tectonophysics, v. 400, p. 241–254, https://doi.org/10.1016/j.tecto.2005.03.006.
Jarrard, R.D., 1986, Terrane motion by strike-slip faulting of forearc sliver: Geology, v. 14, p. 780–783, https://doi.org/10.1130/0091-7613(1986)14<780:TMBSFO>2.0.CO;2.
Jicha, B.R., and Kay, S.M., 2018, Quantifying subduction erosion and the northward migration of volcanism in the central Aleutian arc: Journal of Volcanology and Geothermal Research, v. 360, p. 84–99, https://doi.org/10.1016/j.jvolgeores.2018.06.016.
Kaven, J.O., Maerten, F., and Pollard, D.D., 2011, Mechanical analysis of fault slip data: Implications for paleostress analysis: Journal of Structural Geology, v. 33, p. 78–91, https://doi.org/10.1016/j.jsg.2010.12.004.
Koch, A.J., 1970, Stratigraphy, Petrology, and Distribution of Quaternary Pumice Deposits of the San Cristobal Group, Guatemala City Area, Guatemala [Ph.D. thesis]: Seattle, Washington, University of Washington, 80 p.
Koch, A.J., and McLean, H., 1975, Pleistocene and tephra and ash-flow deposits in the volcanic highlands of Guatemala: Geological Society of America Bulletin, v. 86, p. 529–541, https://doi.org/10.1130/0016-7606(1975)86<529:PTAADI>2.0.CO;2.
Kuiper, K.F., Deino, A., Hilgen, F.J., Krijgsman, W., Renne, P.R., and Wijbrans, J.R., 2008, Synchronizing rock clocks of Earth history: Science, v. 320, no. 5875, p. 500–504, https://doi.org/10.1126/science.1154339.
La Femina, P.C., Dixon, T.H., and Strauch, W., 2002, Bookshelf faulting in Nicaragua: Geology, v. 30, no. 8, p. 751–754, https://doi.org/10.1130/0091-7613(2002)030<0751:BFIN>2.0.CO;2.
LaFemina, P., Dixon, T.H., Govers, R., Norabuena, E., Turner, H., Saballos, A., Mattioli, G., Protti, M., and Strauch, W., 2009, Fore-arc motion and Cocos Ridge collision in Central America: Geochemistry, Geophysics, Geosystems, v. 10, Q05S14, https://doi.org/10.1029/2008GC002181.
Lee, J.-Y., Marti, K., Severinghaus, J.P., Kawamura, K., Yoo, H.-S., Lee, J.B., and Kim, J.S., 2006, A redetermination of the isotopic abundances of atmospheric Ar: Geochimica et Cosmochimica Acta, v. 70, p. 4507–4512, https://doi.org/10.1016/j.gca.2006.06.1563.
Lejri, M., Maerten, F., Maerten, L., and Soliva, R., 2015, Paleostress inversion: A multi-parametric geomechanical evaluation of the Wallace-Bott assumptions: Tectonophysics, v. 657, p. 129–143, https://doi.org/10.1016/j.tecto.2015.06.030.
Logan, J.M., Friedman, M., Higgs, N., Dengo, C., and Shimamoto, T., 1979, Experimental Studies of Simulated Gouge and their Applications to Studies in Natural Fault Zones: U.S. Geological Survey Open-File Report 79-1239, p. 305–343.
Lyon-Caen, H., Barrier, E., Lasserre, C., Franco, A., Arzu, I., Chiquin, L., Chiquin, M., Duquesnoy, T., Flores, O., Galicia, O., Luna, J., Molina, E., Porras, O., Requena, J., Robles, V., Romero, J., and Wolf, R., 2006, Kinematics of the North America–Caribbean–Cocos plates in Central America from new GPS measurements across the Polochic-Motagua fault system: Geophysical Research Letters, v. 33, L19309, https://doi.org/10.1029/2006GL027694.
Mann, P., Rogers, R.D., and Gahagan, L., 2007, Overview of plate tectonic history and its unresolved tectonic problem, *in* Bundschuh, J., and Alvarado, G.E., eds., Central America: Geology, Resources, and Hazards: Milton Park, UK, Taylor and Francis, p. 205–241.
Marrett, R., and Allmendinger, R.W., 1990, Kinematic analysis of fault-slip data: Journal of Structural Geology, v. 12, no. 8, p. 973–986, https://doi.org/10.1016/0191-8141(90)90093-E.
Marrett, R., and Allmendinger, R.W., 1991, Estimates of strain due to brittle faulting: Sampling of fault populations: Journal of Structural Geology, v. 13, no. 6, p. 735–738, https://doi.org/10.1016/0191-8141(91)90034-G.
Marrett, R., and Allmendinger, R.W., 1992, Amount of extension on "small" faults: An example from the Viking graben: Geology, v. 20, p. 47–50, https://doi.org/10.1130/0091-7613(1992)020<0047:AOEOSF>2.3.CO;2.
Martin, K. M., Gulick, S.P.S., Austin, J.A., Jr., Berglar, K., Franke, D., and Udrekh, 2014, The West Andaman fault: A complex strain-partitioning boundary at the seaward edge of the Aceh Basin, offshore Sumatra: Tectonics, v. 33, p. 786–806, https://doi.org/10.1002/2013TC003475.
Martínez-Díaz, J.J., Álvarez-Gómez, J.A., Benito, B., and Hernández, D., 2004, Triggering of destructive earthquakes in El Salvador: Geology, v. 32, no. 1, p. 65–68, https://doi.org/10.1130/G20089.1.
McCaffrey, R., 1992, Oblique plate convergence, slip vectors, and forearc deformation: Journal of Geophysical Research, v. 97, no. B6, p. 8905–8915, https://doi.org/10.1029/92JB00483.
McLean, H., 1970, Stratigraphy, Mineralogy, and Distribution of the Sumpango Group Pumice Deposits in the Volcanic Highlands of Guatemala [Ph.D. thesis]: Seattle, Washington, University of Washington, 99 p.
Michael, A.J., 1984, Determination of stress from slip data: Faults and folds: Journal of Geophysical Research, v. 89, no. B13, p. 11517–11526, https://doi.org/10.1029/JB089iB13p11517.
Min, K., Mundil, R., Renne, P.R., and Ludwig, K.R., 2000, A test for systematic errors in $^{40}Ar/^{39}Ar$ geochronology through comparison with U/Pb analysis of a 1.1-Ga rhyolite: Geochimica et Cosmochimica Acta, v. 64, no. 1, p. 73–98, https://doi.org/10.1016/S0016-7037(99)00204-5.
OpenStreetMap contributors, 2015, Planet Dump [data file from 2018]: https://planet.openstreetmap.org (accessed May 2018).
Patino, L., 2007, Intrusive rocks, *in* Bundschuh, J., and Alvarado, G.E., eds., Central America: Geology, Resources, and Hazards: Milton Park, UK, Taylor and Francis, p. 549–564.
Plafker, G., 1976, Tectonic aspects of the Guatemala earthquake of 4 February 1976: Science, v. 193, no. 4259, p. 1201–1208, https://doi.org/10.1126/science.193.4259.1201.
Reynolds, J.H., 1977, Tertiary Volcanic Stratigraphy of Northern Central America [Master's thesis]: Hanover, New Hampshire, Dartmouth College, 89 p.
Reynolds, J.H., 1980, Late Tertiary volcanic stratigraphy of northern Central America: Bulletin of Volcanology, v. 43, no. 3, p. 601–607, https://doi.org/10.1007/BF02597696.
Reynolds, J.H., 1987, Timing and sources of Neogene and Quaternary volcanism in south-central Guatemala: Journal of Volcanology and Geothermal Research, v. 33, p. 9–22, https://doi.org/10.1016/0377-0273(87)90052-7.

Riller, U., Clark, M.D., Daxberger, H., Doman, D., Lenauer, I., Plath, S., and Santimano, T., 2017, Fault-slip inversions: Their importance in terms of strain, heterogeneity, and kinematics of brittle deformation: Journal of Structural Geology, v. 101, p. 80–95, https://doi.org/10.1016/j.jsg.2017.06.013.

Rodriguez, M., DeMets, C., Rogers, R., Tenorio, C., and Hernandez, D., 2009, A GPS and modelling study of deformation in northern Central America: Geophysical Journal International, v. 178, p. 1733–1754, https://doi.org/10.1111/j.1365-246X.2009.04251.x.

Rose, W.I., Newhall, C.G., Bornhorst, T.J., and Self, S., 1987, Quaternary silicic pyroclastic deposits of Atitlan caldera, Guatemala: Journal of Volcanology and Geothermal Research, v. 33, p. 57–80, https://doi.org/10.1016/0377-0273(87)90054-0.

Rose, W.I., Conway, F.M., Pullinger, C.R., Deino, A., and McIntosh, W.C., 1999, An improved age framework for late Quaternary silicic eruptions in northern Central America: Bulletin of Volcanology, v. 61, p. 106–120, https://doi.org/10.1007/s004450050266.

Sarna-Wojcicki, A., 2000, Tephrochronology, *in* Noller, J.S., Sowers, J.M., and Lettis, W.R., eds., Quaternary Geochronology: Methods and Applications: American Geophysical Union Reference Shelf Series Volume 4, p. 357–377.

Sarna-Wojcicki, A.M., Bowman, H.R., Meyer, C.E., Russell, P.C., Woodward, M.J., McCoy, G., Rowe, Jr., J.J., Baedecker, P.A., Asaro, F., and Michael, H., 1984, Chemical Analyses, Correlations, and Ages of Upper Pliocene and Pleistocene Ash Layers of East-Central and Southern California: U.S. Geological Survey Professional Paper 1293, 22 p.

Schindlbeck, J.C., Kutterolf, S., Freundt, A., Eisele, S., Wang, K.-L., and Frische, M., 2016, Miocene to Holocene marine tephrostratigraphy offshore northern Central America and southern Mexico: Pulsed activity of known volcanic complexes: Geochemistry Geophysics Geosystems, v. 19, p. 4143–4173, https://doi.org/10.1029/2018GC007832.

Scholz, C.H., and Aviles, C.A., 1986, The fractal geometry of faults and faulting, *in* Das, S., Boatwright, J., and Scholz, C.H., eds., Earthquake Source Mechanics: American Geophysical Union Geophysical Monograph 37, p. 147–155, https://doi.org/10.1029/GM037p0147.

Sieh, K., and Natawidjaja, D., 2000, Neotectonics of the Sumatran fault, Indonesia: Journal of Geophysical Research, v. 105, no. B12, p. 28295–28326, https://doi.org/10.1029/2000JB900120.

Staller, A., Martínez-Díaz, J.J., Benito, B., Alonso-Henar, J., Hernandez, D., Hernandez-Rey, R., and Díaz, M., 2016, Present-day crustal deformation along the El Salvador fault zone from ZFESNet GPS network: Tectonophysics, v. 670, p. 66–81, https://doi.org/10.1016/j.tecto.2015.12.017.

Tchalenko, J.S., 1970, Similarities between shear zone of different magnitudes: Geological Society of America Bulletin, v. 81, p. 1625–1640, https://doi.org/10.1130/0016-7606(1970)81[1625:SBSZOD]2.0.CO;2.

Titus, S.J., Housen, B., and Tikoff, B., 2007, A kinematic model for the Rinconada fault system in central California based on structural analysis of en echelon folds and paleomagnetism: Journal of Structural Geology, v. 29, p. 961–982, https://doi.org/10.1016/j.jsg.2007.02.004.

Twiss, R.J., and Unruh, J.R., 1998, Analysis of fault slip inversions: Do they constrain stress or strain rate?: Journal of Geophysical Research, v. 103, no. B6, p. 12205–12222, https://doi.org/10.1029/98JB00612.

Vollmer, F.W., 1995, C program for automatic contouring of spherical orientation data using a modified Kamb method: Computers & Geosciences, v. 21, p. 31–49, https://doi.org/10.1016/0098-3004(94)00058-3.

Vollmer, F.W., 2015, Orient 3: A new integrated software program for orientation data analysis, kinematic analysis, spherical projections, and Schmidt plots: Geological Society of America Abstracts with Programs, v. 47, no. 7, p. 49.

Wallace, R.E., 1951, Geometry of shearing stress and relation to faulting: The Journal of Geology, v. 59, p. 118–130, https://doi.org/10.1086/625831.

Walsh, J., and Watterson, J., 1992, Populations of faults and fault displacements and their effects on estimates of fault-related regional extension: Journal of Structural Geology, v. 14, no. 6, p. 701–712, https://doi.org/10.1016/0191-8141(92)90127-I.

Walsh, J., Watterson, J., and Yielding, G., 1991, The importance of small-scale faulting in regional extension: Nature, v. 351, p. 391–393, https://doi.org/10.1038/351391a0.

Weinberg, R.F., 1992, Neotectonic development of western Nicaragua: Tectonics, v. 11, no. 5, p. 1010–1017, https://doi.org/10.1029/92TC00859.

Weyl, R., 1980, Geology of Central America: Berlin, Borntraeger, 371 p.

Wiesemann, G., 1975, Remarks on the geologic structure of the Republic of El Salvador: Central America: Mitteilungen aus dem Geologisch-Paläontologischen Institut der Universität Hamburg, v. 44, p. 557–574.

Williams, H., 1960, Volcanic history of the Guatemalan Highlands: University of California Publications in Geological Sciences, v. 38, p. 1–86.

Williams, H., and McBirney, A.R., 1969, Volcanic history of Honduras: University of California Publications in Geological Sciences, v. 85, p. 1–70.

Wunderman, R.L., 1982, Amatitlan, an Active Resurgent Caldera Immediately South of Guatemala City, Guatemala [M.S. thesis]: Houghton, Michigan, Michigan Technological University, 213 p.

Wunderman, R.L., and Rose, W.I., 1984, Amatitlan, an actively resurging cauldron 10 km south of Guatemala City: Journal of Geophysical Research, v. 89, no. B10, p. 8525–8539, https://doi.org/10.1029/JB089iB10p08525.

Xu, S.S., Nieto-Samaniego, A.F., and Alaniz-Alvarez, S.A., 2009, Quantification of true displacement using apparent displacement along an arbitrary line on a fault plane: Tectonophysics, v. 467, p. 107–118, https://doi.org/10.1016/j.tecto.2008.12.004.

Žalohar, Z., and Vrabec, M., 2008, Combined kinematic and paleostress analysis of fault-slip data: The multiple-slip method: Journal of Structural Geology, v. 30, p. 1603–1613, https://doi.org/10.1016/j.jsg.2008.09.004.